NTNU – Trondheim
Norwegian University of
Science and Technology

Coherent Plane-Wave Compounding in Medical Ultrasound Imaging

Quality Investigation of 2D B-mode Images of
Stationary and Moving Objects.

Ragnhild Øvland

Master of Science in Physics and Mathematics
Submission date: June 2012
Supervisor: Tore Lindmo, IFY
Co-supervisor: Thor Andreas Tangen, ISB

Norwegian University of Science and Technology
Department of Physics

Preface

This thesis concludes my Master Degree in Physics and Mathematics at the Norwegian University of Science and Technology (NTNU). It was written during the spring of 2012 and submitted on June 12, 2012. The focus of the thesis is medical ultrasound using the coherent plane-wave compounding technique and the advantages and disadvantages of this technique in imaging of stationary and moving objects. The work has been partly programming and simulations and partly *in vitro* and *in vivo* measurements to study the image quality of such images.

This Master's thesis is the continuation of my Specialization Project (TFY4510) written during the autumn of 2011. Some of the background information presented in this report was originally written for my project report.

First and foremost, I would like to thank my supervisor at the Department of Circulation and Medical Imaging (ISB), Thor Andreas Tangen, for support, ideas and mail-answering at all times, and Tore Lindmo, my supervisor at the Department of Physics (IFY), for keeping me on track when writing the report.

I would also like to thank Lasse Løvstakken and Ingvild Kinn Ekroll at the Department of Circulation and Medical Imaging for helpful contributions and Randi Chapana for proof reading.

Lastly, I would like to thank Hanna Koksrud and Solfrid Trydal for making my last year in Trondheim a very good one.

Trondheim, June 12, 2012

Ragnhild Øvland

Sammendrag

Koherent planbølgesammensetning er koherent summasjon av flere suksessive plane bølger som er sendt med ulike sendevinkler. I denne oppgaven presenteres resultater fra simuleringer og *in vitro*- og *in vivo*-målinger av stasjonære og bevegelige objekter, med fokus på tap av oppløsning og kontrast grunnet objektbevegelse. Oppløsning- og kontrastresultater for flere vinkelutvalg, vinkelsekvenser og objekthastigheter og med og uten bevegelseskompensasjon, blir sammenlignet.

Det vises at desimering av vinkleutvalget gir gitterlober som gir dårligere bildekontrast, mens avbilding med en lavere maksimal vinkel gir dårligere lateral oppløsning. Graden av kontrasttap var ulik i simuleringer og målinger.

I simuleringene innebar desimeringsfaktor 2 at kontrasten gikk fra -40 til $-30\,\mathrm{dB}$, mens det for *in vitro*-målingene ikke var signifikant kontrastendring før ved desimeringsfaktor 4. Å bruke et vinkelutvalg desimert med faktor 2 gir en dobling av den oppnåelige bilderaten.

En maksvinkelreduksjon fra 13.7° til 8.2°, som tilsvarer å endre sende-F-tallet fra 2.1 til 3.5, gir i underkant av 0.3 mm reduksjon av lateral oppløsning, for oppløsninger rundt 1 mm. Dette øker bilderaten med en faktor 1.2.

For punktspredere gir aksiale sprederhastigheter vesentlig dårligere bildekvalitet enn for stasjonære spredere, mens effekten av laterale sprederhasdtigheter er begrenset. I hvilken grad oppløsning og kontrast blir redusert på grunn av bevegelse avhenger av utvalget av plane bølger som inngår i hvert bilde, og sekvensen bølgene blir sendt ut i. Å bruke en undermengde av det optimale vinkelsettet førte til forbedring for desimeringfaktor 4 ved en aksiell hastighet på 10.0 cm/s, men ikke for desimeringfaktor 2, selv om den totale bevegelsen per bilde ble redusert som følge av færre utsendte planbølger. Kvalitetstapet grunnet bevegelse var gjerne lavere ved færre planbølgevinkler, men den totale kvaliteten var likevel dårligere for mange av disse vinkelsettene på grunn av gitterlober.

For *in vivo*-opptak var ikke effekten av bevegelse like tydelig, og det virker lovende å jobbe videre med koherent planebølgesammensetning også for bevegelige objekter.

Abstract

Coherent plane-wave compounding is the coherent summation of several successive plane waves incident at different angles. This thesis presents results from simulations and *in vitro* and *in vivo* measurements of stationary and moving objects, with focus on loss of resolution and contrast due to object motion. Resolution and contrast results for several angle selections, angle sequences and object velocities with and without motion correction have been compared.

It is shown that using a subset of plane-wave tilt angles by decimating the optimal selection introduces grating lobes which degrades the image contrast, while imaging with a lower maximum tilt angle degrades the lateral resolution.

The contrast loss for decimation factor 2 was more significant for simulations than for *in vitro* measurements. While the contrast went from -40 to -30 dB for the simulations, a decimation factor of 4 was needed to degrade the contrast significantly for the measurements. Decimating the angle selection by a factor of 2 doubles the achievable frame rate.

A reduction in maximum angle from 13.7° to 8.2°, which corresponds to an increase in transmit F-number from 2.1 to 3.5, gives less than 0.3 mm degradation of lateral resolution. The lateral resolution is of the order of 1 mm. This reduction in maximum angle increases the frame rate by a factor of 1.2.

Axial point scatterer velocity leads to considerably worse image quality than for stationary scatterers, while the effect of lateral scatterer velocities is limited. The degree of contrast and resolution loss due to object motion is dependent on the selection of plane waves which constitute a frame, and the sequence in which the plane waves are transmitted. Using a subset of the optimal angle selection leads to improvement in image quality for an axial velocity of 10.0 cm/s for decimation factor 4, but not for decimation factor 2, even though the total scatterer movement per frame is reduced by the reduction of transmitted plane-waves. The loss of quality due to motion was less for fewer tilt angles, but the total image quality was still worse for many of these sets of angles due to grating lobes.

The unwanted effects of motion for *in vivo*-measurements were not seen to the same extent as for simulated point scatterers, and working with the coherent plane-wave compound seems promising for moving objects.

Contents

List of Figures

List of Tables

List of Abbreviations

AP	Alternating polarity angle sequence
bpm	Beats per minute
bps	Beats per second
CCC	Cross correlation correction
et al.	et alii; and others
$F_{\#}$	F-number
fps	Frames per second
IQ	In phase/Quadrature
LA	Linear angle sequence
PRF	Pulse repetition frequency
RF	Radio frequency

1 Introduction

Coherent plane-wave compounding was first mentioned in 2004 [1] and studied by Montaldo et al. in 2009 [2] as an alternative beamforming technique to the conventional fixed-focus transmit beams. Instead of a single transmitted fixed-focus beam for each scan line, plane waves tilted at different angles are transmitted in sequence. By applying proper delays on the received signal, synthetic transmit focusing is achieved at all points in the image. Because the same plane waves are used to beamform the entire image, this is possible without reducing the frame rate, as opposed to fixed-focus imaging where multiple focus depths must be used to achieve a similar effect.

Contrary to ultrafast imaging techniques such as single plane wave imaging which increases frame rate at the cost of image quality, the coherent plane-wave compound reduces the number of necessary transmissions per frame without reducing image quality. In addition to the focusing ability, transmitting plane waves at several angles to the tissue may give improvement in the imaging of tissue in cases of angular dependent scattering.

A high frame rate is desired because it allows visualization of rapidly moving objects, such as the heart. The use of small animals in cardiovascular imaging is increasing, and consequently, so is the demand for adequate methods for imaging of hearts with very fast heart rates. To recognize motion details and to enable quantitative measurements, the imaging frame rate must be sufficiently high compared to the heart rate.

For cardiac imaging, measuring and visualizing blood flow using Doppler techniques is extensively used. For duplex or triplex imaging, which shows blood velocities together with a B-mode image of the heart, the Doppler sequences must be acquired in between the acquisition of the B-mode images. This reduces the number of Doppler transmissions, which either reduces filtering possibilities due to fewer transmissions in each direction (reduced packet size) or the size of the imaged area. With plane-wave compounding, Doppler and B-mode images can be acquired simultaneously, which allows large packet sizes and a Doppler area equal to the entire imaged area.

Unfortunately, compared to conventional imaging, the coherent plane-wave compounding technique is especially sensitive to motion. In conventional B-mode imaging, a single transmitted wave is used to form a scan line, and hence motion along this line does not affect the image. In the plane-wave method, on the other hand, plane waves fired at different times are combined to form the individual image lines. Thus, tissues moving fast compared to the pulse repetition rate move substantially between waves which are later combined to form a single line. Because moving scatterers induce a phase shift between successive insonifications, this leads to degraded image quality.

Previously, the coherent plane-wave method has been investigated for transient elastography [2], in which shear waves induces tissue motion which can be measured to find the Young's modulus of the tissue, and for Doppler imaging of blood flow [5]. However, to the author's knowledge, no research has been published on the effect of

motion on the quality of B-mode images acquired using this technique.

The objective of the present report is to investigate the effect of motion on coherent plane-wave compounding. As a means to reduce motion artifacts and increase frame rate, the effect of reducing the number of transmitted waves per frame for stationary scatterers is also investigated, in addition to moving objects.

This report presents simulated *in vitro* and *in vivo* results from plane-wave acquisitions of stationary and moving scatterers. The presented results are divided into three main parts. The first part presents simulations and *in vitro* measurements of stationary scatterers which compares the coherent plane-wave compounding method to the more conventionally fixed-focus imaging method. This part also contains results from simulations and measurements using a reduced number of transmission angles. Then, a second part presents simulations of moving scatterers and the effect of motion on image quality. An attempt is made to reduce the effect by motion correction. The last part includes *in vivo* results from imaging of a young rat's heart, both using the fixed-focus method and variants of the coherent plane-wave compound.

2 Background

Ultrasound in general is sound with frequencies higher than the human hearing range, or above 20 kHz. Frequencies in medical ultrasound typically range from 2 to 15 MHz [6]. In ultrasound imaging, sound pulses are transmitted by a transducer which converts electric voltage to longitudinal sound waves, and the pulses are reflected or scattered in the tissue. The reflected pulses are again converted to electric voltage by the transducer and processed to form an image. Because there is little variation in the speed of sound in human tissue, time in the received signal is linearly related to distance from the transducer. The amplitudes of the received echoes give information about differences in acoustic impedance. In 2D-ultrasound using 1D-arrays, the two main coordinate axes are the axial or z-direction down into the tissue from the transducer, and the lateral or x-direction along the length of the transducer. In the elevation direction, y, fixed focusing is applied using an acoustic lens.

2.1 Transducers

Ultrasound array transducers consist of multiple piezoelectric elements which are compressed and expanded in the thickness dimension when voltage is applied [7]. The compression and expansion of the elements cause displacement which propagates through the medium coupled to the transducer.

A linear array consists of 48-128 elements [6, 8] which transmit and receive independently. In the elevation direction, the beam has a static focus using an acoustic lens, whereas the elements in the lateral direction achieve focusing by using time delays to the individual elements. The delays ensure constructive and destructive interference between pulses from different elements, which is used to concentrate the energy at a focal point. Each element has a width of $\lambda/2$ to $3\lambda/2$, where λ is the wavelength of the center frequency of the transducer. The distance between the midpoint of two elements, the pitch, is slightly longer than the width of the elements. In a linear array, a subset of elements centered around the imaged line is used on transmit. A delay is applied to the individual elements, such that an element with no delay transmits before an element with a large delay.

2.2 Wave field

The individual transmitted sound pulses from each transducer element are a few periods of sine waves with varying phase according to time and distance from the element. Waves with large phase differences have destructive interference. The far field is defined as the region where the phase difference between waves from two transducer elements is less than $\pi/4$ [9], which ensures positive interference between waves from different elements at all positions. This is the case beyond a distance $R_c = \frac{a^2}{\lambda}$ from the transducer, where a is the active aperture size and λ is the center wavelength of the waves. Unfortunately, for transducers used in medical imaging,

the far field limit R_c is of the order of 1 m. This necessitates some kind of focusing to control the relative phase of the sound waves at closer ranges.

2.3 Beamforming

Beamforming is a signal processing technique to control the steering and focusing of array transducers [10, 11]. For focusing, the objective of the beamformer is to apply appropriate delays to the individual elements in order to achieve maximum constructive interference in the focal point. The delays vary according to the depth of the focal point. While a transmit beam can only focus at a single depth, dynamic receive focusing is possible, as the signal from larger depths return later than signal from closer points.

2.3.1 F-number

The resolution of an image is related to the F-number [6], which is defined as the ratio of focus depth to active transducer aperture size. A lower F-number yields a narrower beam (improved lateral resolution) and shorter depth of field, while a higher F-number produces a wider beam with a longer depth of field. For a fixed focus a moderate F-number is usually applied in order to ensure a longer focal region, while lower F-numbers are used for dynamic focusing. To keep the resolution as constant as possible throughout the image, a constant F-number is desired. When focusing on receive, a larger number of receive channels are used with increasing focus depth to keep the F-number constant. Usually, the transducer width limits the aperture size for the largest depths. For very shallow foci, a minimum number of elements is used to ensure enough signal reception.

2.3.2 Apodization

Apodization is amplitude weighting which reduces side lobes at the expense of a broader main lobe [7]. Transmit apodization is implemented by transmitting pulses of varying voltage from the individual elements. On receive, apodization is introduced as weighting factors on the separate receive elements. When a certain line is formed, the signal from elements further away from this line have less weight than the signal from closer transducer elements. This decreases the influence of the elements most likely to be influenced by reflections from other lateral positions. Usual apodization windows include Hamming, Hanning and cosine filters.

2.3.3 Data flow

On receive, the sound waves are converted to an analog signal by the transducers, and the signal for each receive channel is further converted to a digital signal through an analog-to-digital converter (ADC). Most ADCs used today use 12 bits for each sample, at a rate of 40Msamples/s [12]. For 128 channels, this equals $61 \cdot 10^9$ bits/s, or 7.2 GB/s, about the contents of a DVD per second. In clinical scanners, the data flow is reduced as quickly as possible by the beamformer. In research scanners,

when flexible beamforming is required, it is advantageous to collect pre-beamformed signals and do beamforming later. This is very demanding of the system, as all data must be stored and transported through the system.

2.4 Frame rate

The frame rate is the rate of acquisition of each frame, meaning a full image. The frame rate is limited by the depth of the imaging region and the number of necessary transmitted beams per frame. Sound waves travel at the speed of sound, c $\approx$ 1540 m/s, in tissue [6]. Thus, the required time from emission of a beam until reception of the reflected signal from a point at depth z_{max} is $T_{max} = \frac{2z_{max}}{c}$. $PRF_{max} = \frac{1}{T_{max}}$, the maximum pulse repetition frequency, is the highest possible rate of pulse transmission. If n beam transmissions are needed to complete a frame, the frame rate equals PRF_{max}/n.

2.5 IQ-demodulation

IQ-demodulation, or quadrature demodulation, is the separation of a signal into its in-phase and quadrature components [13, 14]. The IQ-demodulation of a real signal of a certain bandwidth is a shift in frequency, usually down to 0 Hz for the central frequency. The resulting data is complex-valued, and has a maximum frequency equal to half the bandwidth of the signal.

The signal from an ultrasound transducer is called an RF-signal, or radio-frequency signal. This is a real signal with a certain bandwidth covering the center transmit frequency. According to the Nyquist sampling theorem [15], this signal must be sampled with a frequency which is twice the highest frequency component of the signal. Thus, IQ-demodulation reduces the necessary sampling frequency without loss of information, as the information from the original real signal is contained in the phase and amplitude of the IQ-signal.

To display an image, the phase is no longer important and the envelope (absolute value) of the signal is taken before the image is displayed. When combining signals from different elements or beams, the summation is called coherent compounding when it is performed before the phase information is removed (Fig. 1a) and incoherent compounding if envelopes are summed and phase information is neglected (Fig. 1b).

2.6 Correlation

The cross correlation between two discrete signals $x_i(k)$ and $x_j(k)$ of length N is given by [6, 15]

$$C_{ij}(n) = \frac{1}{N} \sum_{k=0}^{N-1} x_i(k) \cdot x_j^*(k+n). \tag{1}$$

$x_j^*(k+n)$ is the complex conjugate of $x_j(k+n)$. The value of n which gives the maximum C_{ij} corresponds to the lag between x_i and x_j which gives the best fit.

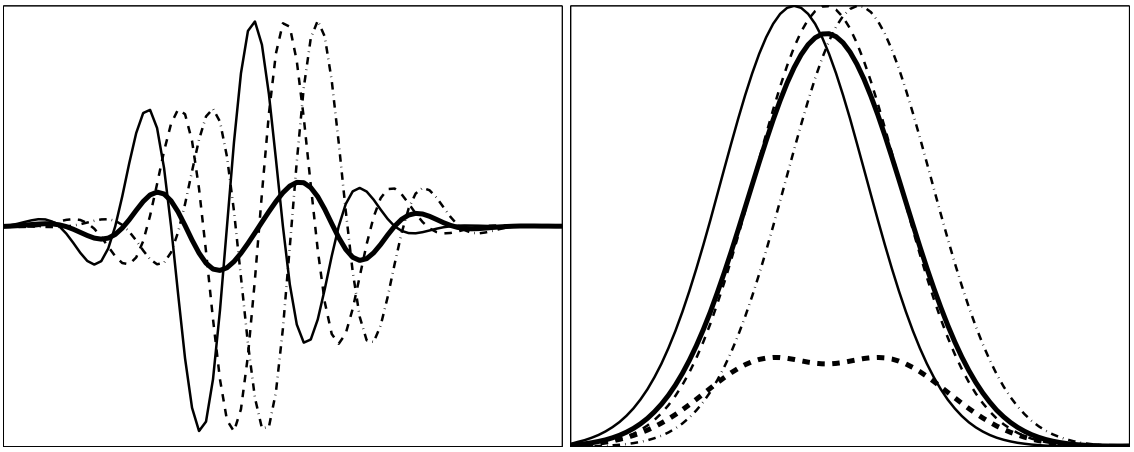

(a) Coherent compounding (b) Incoherent compounding

Figure 1: Compounding of signal from three separate transmissions reflected off a moving scatterer. (a) Illustration of coherent summation. RF-signal of all transmissions shown together with coherent sum (thick, solid line). The phase displacement causes considerable loss of amplitude. (b) The envelopes of all signals are shown, together with the incoherently summed signal (thick, solid line) and the envelope of the coherently summed signal (thick, dashed line). There is little loss of amplitude for the incoherent summation. Both summed envelopes have been divided by 3 to be compared to the original envelopes.

At a lag of $n = 0$, the cross correlation can be used to estimate the phase difference between $x_i(k)$ and $x_j(k)$ at sample k_0 [16].

$$< C_{ij} =< \left(\frac{1}{2m+1} \sum_{k=k_0-m}^{k_0+m} x_i(k) \cdot x_j^*(k) \right) \approx < x_i(k_0) - < x_j(k_0) \tag{2}$$

The normalized correlation, ρ, can be used to determine the degree of correlation. It is calculated as

$$\rho = \frac{|C_{ij}|}{\sqrt{|C_{ii}||C_{jj}|}} \tag{3}$$

2.7 Fixed-focus imaging

A much used imaging modality in medicine is 2D B-(brightness) mode imaging. This is a gray scale image showing the intensity of the received signal, which corresponds to the square of the signal envelope (section 2.5). Bright areas in the image are the result of high reflection amplitudes. B-mode images from clinical scanners today are usually acquired using fixed-focus beams. For a linear array transducer, one beam is transmitted for each line of the finished image. To achieve full resolution, the lateral sampling must fulfill the Nyquist sampling criteria, which requires less than $\frac{\lambda F_\#}{2}$ [7] between each scan line. For an aperture of 4 cm, with an F-number of 2 and frequency 6.67 MHz, this requires 173 lines per frame. Each beam consists of pulses

from a sub-aperture of the total transducer, about 30-60 elements. The elements in the middle of the aperture are delayed more than the elements on the sides because of differences in travel time to the desired focal point, as shown in Fig. 2. The distance from tranducer element n to the focal point (x_f, z_f) is longer than for the central element m, hence the pulse from element n needs a head start, accomplished by holding back the pulse from element m.

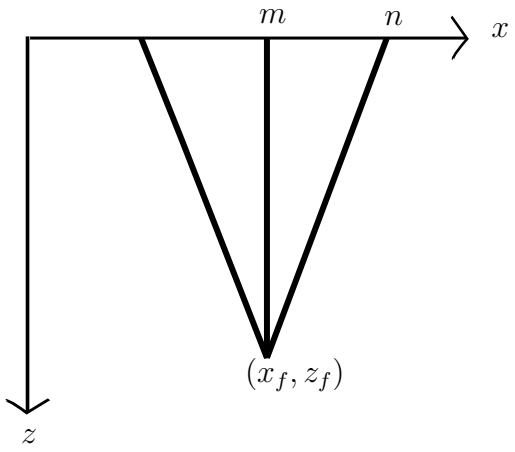

Figure 2: Time of flight in fixed-focus imaging. The transmit beams are focused to be in phase at the focal point (x_f, z_f) by delaying pulses from element m longer than pulses from element n.

Images using this method show good resolution at the focal depth, but the resolution decreases rapidly away from this depth. To compensate for the decreasing quality, it is possible to acquire several images with different focal depths and combine them. However, as a new image must be acquired for each focal depth, this reduces the frame rate by a factor equal to the number of foci. The depth of field for a focused wave is $\Delta z = 7\lambda F_{\#}^2$ [17], which for beams with frequency 6.67 MHz and F-number 2 corresponds to about 6 mm. An optimal multifocal system should have one focal point for each depth of field, giving 10 foci for a 6 cm deep image. In practical use, the number of foci is often limited to four or less, to maintain an acceptable frame rate.

Although only a single focal depth is possible on transmit, dynamic focusing is applied on receive. As described in section 2.3, reflections from tissue close to the transducer arrive earlier than reflections from larger depths. This enables different delays for the different depths, resulting in receive focusing on all depths or several depth regions.

2.8 Plane-wave imaging

An alternative to transmitting focused waves is imaging using plane waves. This means to transmit on all elements without focusing delays to cover the whole area to be imaged with a single wave. If one wave is sufficient to create an image frame, the

frame rate is equal to the pulse repetition rate and can reach 20 kHz, depending on the maximum imaging depth. The concept has been studied since the late 70's, when the research group of Delannoy, Bruneel, Bridoux, Rouvaen and Torguet attempted to make the acoustical lateral focusing lens which was used then, redundant [3, 4]. The lens made it impossible to rapidly change the focus depth of the beams. Their solution was to transmit plane, unfocused waves and use parallel processing on receive. The technology available to Bruneel et al. at that time was limited in both the electronics and the processing power.

Others have explored new methods to utilize plane waves in imaging, such as Lu [19, 20], who studied plane waves as a special case of limited diffraction beams, and Hu et al. [21], who presented a method to increase the resolution of single plane wave images by using a combination of a filter for retrospective transmit focusing and filter-based weighting.

2.9 Coherent plane-wave compounding

Coherent plane-wave compounding is the coherent addition of signal from several plane waves. The plane waves, which are tilted at different angles, are transmitted successively and the received signal is later combined.

Coherent plane-wave compounding was first proposed by Song and Chang in 2004 [1], and Cheng and Lu [22] extended in 2006 the single plane wave method of the latter [20] to include both coherent and incoherent compounding of multiple plane waves. An extensive investigation of coherent compounding was given by Montaldo et al. in 2009 [2]. They showed that the resultant pressure field from coherent summing of properly delayed plane waves equals the pressure field at the focal depth of a fixed-focus wave.

2.9.1 Beamforming

The received signal from the individual plane-wave transmissions is delayed by the transmit and receive delays τ_t and τ_r, as presented below, before summation. The receive delay are identical to the dynamic receive delays applied in the fixed-focus acquisition method. The transmit delays account for the transmission at different angles, ensuring that the phase at a certain focal point is equal for all transmissions. Because the phase alignment is made by delays to the received signal, they can be varied for all points in the image to give constructive interference and focusing at all points.

There are no transmit focusing delays applied on transmit, as is the case for the fixed-focus method, but in order to transmit at an angle other than perpendicular to the transducer, some delays must be added. This can be thought of as firing all elements at the same time, but along an imaginary axis x' at an angle θ to the transducer, as shown in Fig. 3. The x-axis is along the transducer surface, measured from the middle of the first element. The delays applied on the elements on transmission correspond to the distance a from x' to x and is dependent on θ and the position of the element, x_e.

$$\tau_{\theta,x_e}(\theta, x_e) = \frac{x_e \cdot \sin(\theta)}{c}, \tag{4}$$

c is the speed of sound in tissue.

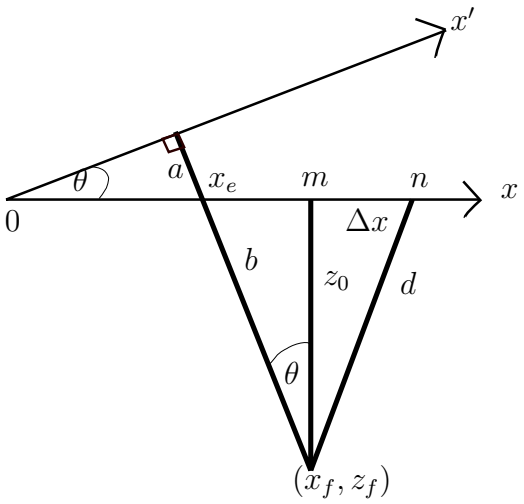

Figure 3: Beam transmission of a plane wave at an angle θ. Beams are transmitted from the imaginary axis x' at a time t_0. x-axis is along the transducer surface. The origin is in the middle of the leftmost element.

The transmit and receive focusing delays τ_t and τ_r applied by delaying the received signal can also be found using Fig. 3. The wavefront of a wave must travel a distance $s_t = a + b$ from transmission to reach position (x_f, z_f) which gives

$$\begin{aligned} \tau_t(x_f, z_f, \theta) &= \frac{a+b}{c} \\ &= \frac{x_f \sin\theta + z_f \cos\theta}{c}. \end{aligned} \tag{5}$$

A wave scattered off a point in position (x_f, z_f) must travel a distance $s_r = d$ to reach element n in position $(x_f + \Delta x, 0)$, and the corresponding delay is

$$\begin{aligned} \tau_r(z_f, \Delta x) &= \frac{d}{c} \\ &= \frac{\sqrt{z_f^2 + \Delta x^2}}{c}. \end{aligned} \tag{6}$$

Although each plane wave is transmitted individually, the coherent compounding of the received signal makes the total pressure field from the summation of the plane waves instructive in the description of the resulting image. Montaldo et al. [2] derives an expression for this pressure field p, which in position (x, z) of plane

waves synthetically focused at (x_f, z_f), can be expressed as the sum of the individual pressure fields p_n for plane waves delayed with the transmit delays τ_t

$$\begin{aligned} p(x, z, x_f, z_f, t) &= \sum_n p_n(x, z, t + \tau_t(x_f, z_f, \theta_n)) \\ &= \sum_n p_0 \exp j(k_x^n x + k_z^n z - \omega(t + \tau_t(x_f, z_f, \theta_n))), \end{aligned} \tag{7}$$

where

$$\begin{aligned} k_x^n &= k \sin(\theta_n), \\ k_z^n &= k \cos(\theta_n) \end{aligned} \tag{8}$$

and

$$k = \frac{2\pi}{\lambda}.$$

At the focal depth z_f, in coordinates $(x', z') = (x - x_f, z - z_f)$,

$$\begin{aligned} p(x', z', t) &= \sum_n p_0 \exp j \left(k_x^n x + k_z^n z - w \left(t + \frac{x_f \sin\theta_n + z_f \cos\theta_n}{c} \right) \right) \\ &= \sum_n p_0 \exp j(k_x^n (x - x_f) + k_z^n (z - z_f) - \omega t) \\ &\overset{z=z_f}{=} \sum_n p_0 \exp j(k_x^n x' - \omega t). \end{aligned} \tag{9}$$

The appropriate angles are chosen based on the spatial sampling frequency in the lateral direction given by the transducer pitch, dx. The spatial frequency spectrum has a width equal to the sampling frequency, $\frac{2\pi}{dx}$. The M transducer elements ensures M uniformly spaced, independent k_x-values to be fitted into this interval, giving

$$k_x^n = \frac{2\pi n}{M \cdot dx} = \frac{2\pi n}{L}, \qquad n = -\frac{M}{2}, \ldots, \frac{M}{2} - 1. \tag{10}$$

L is the width of the transducer. Inserting the spacial frequencies into (9), including only the $N \leq M$ (N odd) central frequencies and allowing for transmit apodization weights w_n, the sum can be computed as

$$\begin{aligned} p_{\text{plane}}(x', z' = 0, t, N) &= \sum_{n=-\frac{N-1}{2}}^{\frac{N-1}{2}} p_0 \exp(-j\omega t) w_n \exp\left(j \frac{2\pi x' n}{L} \right) \\ &= p_0 \exp(-j\omega t) \sum_{n=-\frac{N-1}{2}}^{\frac{N-1}{2}} w_n \exp\left(j \frac{2\pi x' n}{L} \right) \\ &= p_0 \exp(-j\omega t) W_{\text{plane}}(x'), \end{aligned} \tag{11}$$

where the sum is the discrete Fourier transform W_{plane} of the weights w_n. Setting the apodization weights to unity gives the Fourier transform of a rectangle [15]

$$p_{\text{plane}}(x', z' = 0, t, N) \overset{w_n=1}{=} p_0 \exp(-j\omega t) \frac{\sin(\frac{\pi x' N}{L})}{\sin(\frac{\pi x'}{L})}. \tag{12}$$

The pressure field for a fixed-focus beam [6, 7] from an aperture of M elements with transmit apodization weights w_m is, at the focal depth, given by

$$\begin{aligned} p_{\text{focused}}(x', z' = 0, t, M) &= \sum_{m=-\frac{M}{2}}^{\frac{M}{2}-1} p_f \exp(-j\omega t) w_m \exp\left(j \frac{kx'dxm}{z_f}\right) \\ &= p_f \exp(-j\omega t) \sum_{m=-\frac{M}{2}}^{\frac{M}{2}-1} w_m \exp\left(j \frac{kx'dxm}{z_f}\right) \\ &= p_f \exp(-j\omega t) W_{\text{focused}}(x'), \end{aligned} \tag{13}$$

where again the sum is the Fourier transform W_{focused} of the weights w_m. As for the plane wave case, uniform apodization gives the Fourier transform of a rectangle.

$$p_{\text{focused}}(x', z' = 0, t, M) \overset{w_i=1}{=} p_f \exp(-j\omega t) \frac{\sin(\frac{kx'L}{2z_f})}{\sin(\frac{kx'dx}{2z_f})} \exp\left(\frac{-jkx'dx}{2z_f}\right), \tag{14}$$

Comparing the sines in the numerator of the two expressions in (12) and (14), the number of compounded plane waves N is equal to

$$N = \frac{\frac{\pi x' L}{\lambda z_f}}{\frac{\pi x'}{L}} = \frac{L}{F_{\#}\lambda}. \tag{15}$$

The transmit angles which yields adequate lateral sampling are given by (8), (10) and (15) as

$$\theta_n = \sin^{-1}\left(\frac{\frac{2\pi n}{L}}{\frac{2\pi}{\lambda}}\right) = \sin^{-1}\left(\frac{\lambda n}{L}\right) \approx \frac{\lambda n}{L}, \qquad n = -\frac{N-1}{2}, \ldots, \frac{N-1}{2}. \tag{16}$$

Combining (15) and (16) gives

$$F_{\#} = \frac{L}{N\lambda} = \frac{1}{N\delta\theta} = \frac{1}{\theta_{max}}. \tag{17}$$

Thus, the F-number of coherent plane-wave compounding acquisitions is dependent on the maximum transmit angle used only. A higher maximum angle, which means more tilted waves, corresponds to a low F-number.

In order to reduce the number of transmitted plane waves per frame, the set of transmit angles may be decimated by a decimation factor D. Returning to (11) to investigate the new pressure field at focal depth,

$$\begin{aligned} p(x', z' = 0, t, N, D) &= \sum_{n=-\frac{(N-1)/D}{2}}^{\frac{(N-1)/D}{2}} p_0 \exp(-j\omega t) w_n \exp\left(j\frac{2\pi x' D n}{L}\right) \\ &= p_0 \exp(-j\omega t) \sum_{n=-\frac{(N-1)/D}{2}}^{\frac{(N-1)/D}{2}} w_n \exp\left(j\frac{2\pi x' D n}{L}\right) \\ &\overset{w_i=1}{=} p_0 \exp(-j\omega t) \frac{\sin(\frac{\pi x'(N+(D-1))}{L})}{\sin(\frac{\pi x' D}{L})}. \end{aligned} \tag{18}$$

The only changes to the pressure field by decimating the set of angles is $N \Rightarrow N + (D-1) \approx N$ in the numerator, and in the denominator where the argument of the sine is multiplied by the decimation factor. For small values of $\frac{\pi x' D}{L}$ this sine can be approximated by its argument, giving

$$\begin{aligned} p(x', z' = 0, t, N, D) &\approx p_0 \exp(-j\omega t) \frac{\sin(\frac{\pi x' N}{L})}{\frac{\pi x' D}{L}} \\ &= p_0 \exp(-j\omega t) \frac{N}{D} \operatorname{sinc}\left(\frac{\pi x' N}{L}\right). \end{aligned} \tag{19}$$

Hence, provided that the approximation holds, the pressure field at the focal depth is a sinc-function for both the complete ($D = 1$) and the decimated ($D > 1$) angle set. The pressure field is reduced in amplitude by a factor equal to the decimation factor D, consistent with the reduction of transmitted waves by a factor D.

Referring to Fig. 4, the sinc-approximation does not hold beyond $x' \approx \frac{L}{2D}$. Because of the reduced lateral sampling due to decimation, aliasing artifacts occur.

The main lobe of the sinc-function has a halfwidth of $x' = \frac{L}{N} < \frac{L}{2D}$ and is a good approximation for all $D < \frac{N}{2}$. However, the expression in (18) has a maximum when the sine in the denominator is zero, for $\frac{\pi x' D}{L} = p \cdot \pi$, where p is an integer. Thus grating lobes will appear for $x' = \frac{Lp}{D}$, as seen in Fig. 4.

Using an apodization window other than the uniform window, the side lobes seen for all decimations factors in Fig. 4 can be reduced, but the grating lobes cannot be reduced by apodization.

2.10 Motion artifacts

The synthetic focusing of the coherent plane-wave compound is based on the coherent summation of signals from position (x_0,z_0) from several waves transmitted at

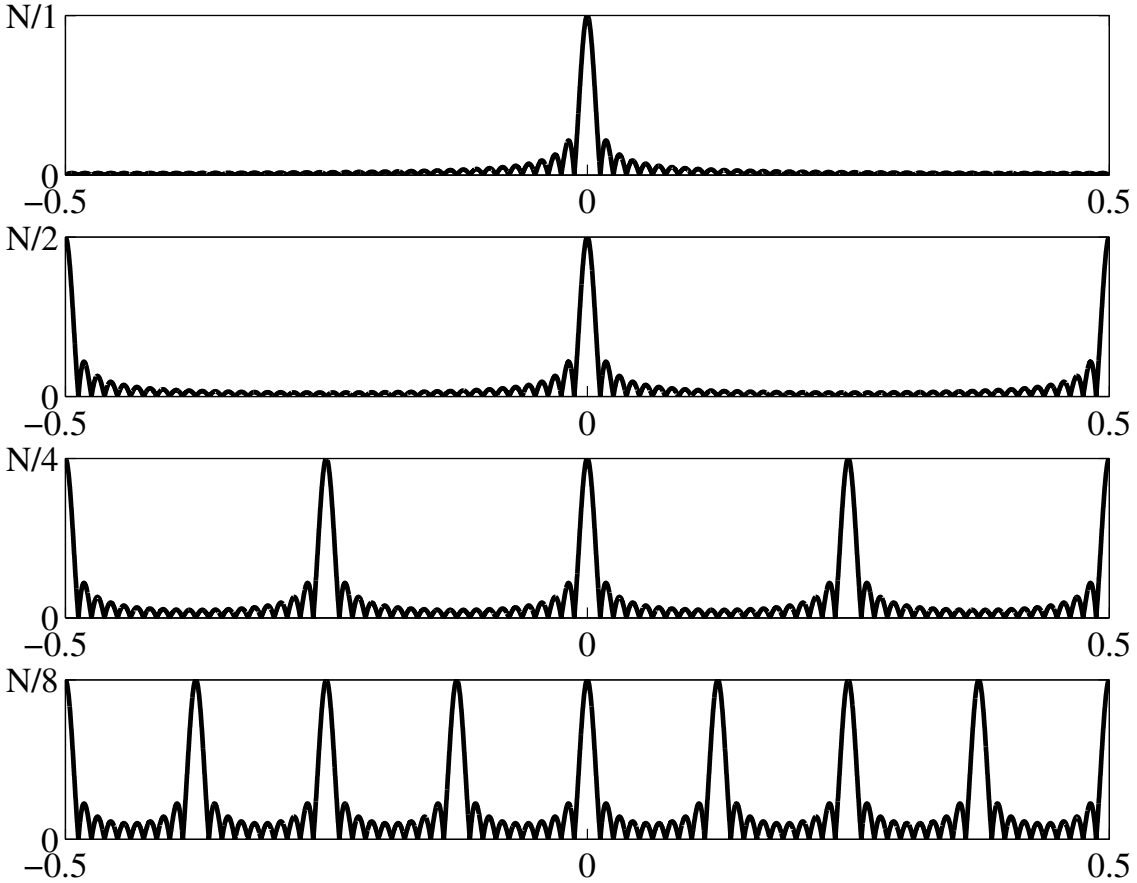

Figure 4: The combined pressure field $|p/p_0|$ using N transmit angles plotted for decimations factors 1, 2, 4 and 8 as a function of x'/L.

different times. This requires that the object is stationary between illuminations for each of the plane waves. With the inclusion of motion, this is no longer the case. This will lead to a blurring of moving scatterers, as the scatterers will have different positions at the different plane-wave transmissions.

For a downward scatterer velocity of 10 cm/s, using a PRF of 12 kHz, the scatterer displacement between two transmissions is 8.3 µm. Compared to the axial resolution, which at a frequency of 6.7 MHz with a 2 period pulse, corresponds to 229 µm, this displacement is negligible. Thus, if the envelopes are summed incoherently such as for the solid line in Fig. 1b, a slight blurring of the scatterer due to the misalignment of the envelopes would be the only effect of motion.

However, in coherent compounding, the phase information is still intact when the summation is performed. Thus, the scatterer displacement must instead be compared to the wavelength of the returning pulse, which is half the wavelength of the original pulse, or 115 µm. As illustrated in Fig. 1a, a phase difference of π between two consecutive transmissions, corresponding to a displacement of 115 µm/2 = 57 µm, causes destructive interference and a significant reduction in combined intensity. The total phase difference from the first to the last transmission in a

frame should be as small as possible to minimize such amplitude reduction. The phase difference from the first to the middle transmitted wave can be calculated as

$$\phi = \frac{N-1}{2} \cdot \frac{v/PRF}{\lambda/2} \cdot 2\pi. \tag{20}$$

Thus, to ensure a phase difference between first and middle transmitted wave for 81 angles of less than π, the maximum velocity is

$$v_{max} = \frac{\phi_{max}}{2\pi} \cdot \frac{2}{N-1} \cdot PRF \cdot \lambda/2 = \frac{\pi}{2\pi} \cdot \frac{1}{40} \cdot 12\,\text{kHz} \cdot 57\,\mu\text{m} = 8.6\,\text{mm/s}. \tag{21}$$

For only 11 angles, this maximum velocity is 68.4 mm/s.

In the lateral direction, the scatterer displacement should be compared to the lateral resolution. As this is of the order of $F_\# \cdot \lambda \approx 450\,\mu\text{m}$, the effect of motion is expected to be less prominent for lateral motion than for axial motion. However, a lateral velocity of 10 cm/s, resulting in a shift of 670 µm for 81 waves, will be noticeable.

2.10.1 Angle sequence

For stationary scatterers the sequence in which the differently tilted waves are transmitted does not matter. For moving scatterers, this is of importance. Each transmitted plane wave incident on a point scatterer results in edge waves tilted in the same way as the original wave relative to horizontal waves (Fig. 5a). For a stationary scatterer, all edge waves are centered at the scatterer position (Fig. 5b). When an object moves between transmissions, the transmission sequence determines the interference pattern created by the compounding of several edge waves. As the signal from the individual waves is coherently compounded, the intensities of edge waves are not added directly, as it seems to be in Fig. 5. This is a simplification to explain a phenomenon due to constant axial motion.

Two possible transmit sequences are the linear (LA) and alternating polarity (AP) sequences. LA means transmitting plane waves with linearly varying tilt angles,
$[-a_N, -a_{N-1}, \ldots, 0, \cdots, a_{N-1}, a_N]$, while the AP sequence transmits waves with alternating positive and negative tilt angles, $[0, -a_1, a_1, \ldots, -a_N, a_N]$. For point scatterers moving at constant axial velocity, some interesting artifacts occur. For the LA sequence, because of the constant angular spacing between successive waves combined with the constant axial velocity, all edge waves from the individual waves meet at two points to the side of the scatterer, as illustrated in Fig. 5c. The axial displacement of the scatterer between transmissions moves the center of the edge waves, while the varying transmit angles tilt the waves.

For the AP sequence, the effect is less visible in Fig. 5d because of the varying spacing between successive tilt angles. The effect is present, but on both sides of the scatterer and at about twice the distance to the scatterer. In this case, the positive and negative angles will act as two separate LA sequences.

In the AP sequence, there is little movement between to equal angles of opposite polarity, which leads to an approximately symmetric point spread function. For the LA sequence, there is much motion between opposite angles, which makes the point spread function more asymmetric.

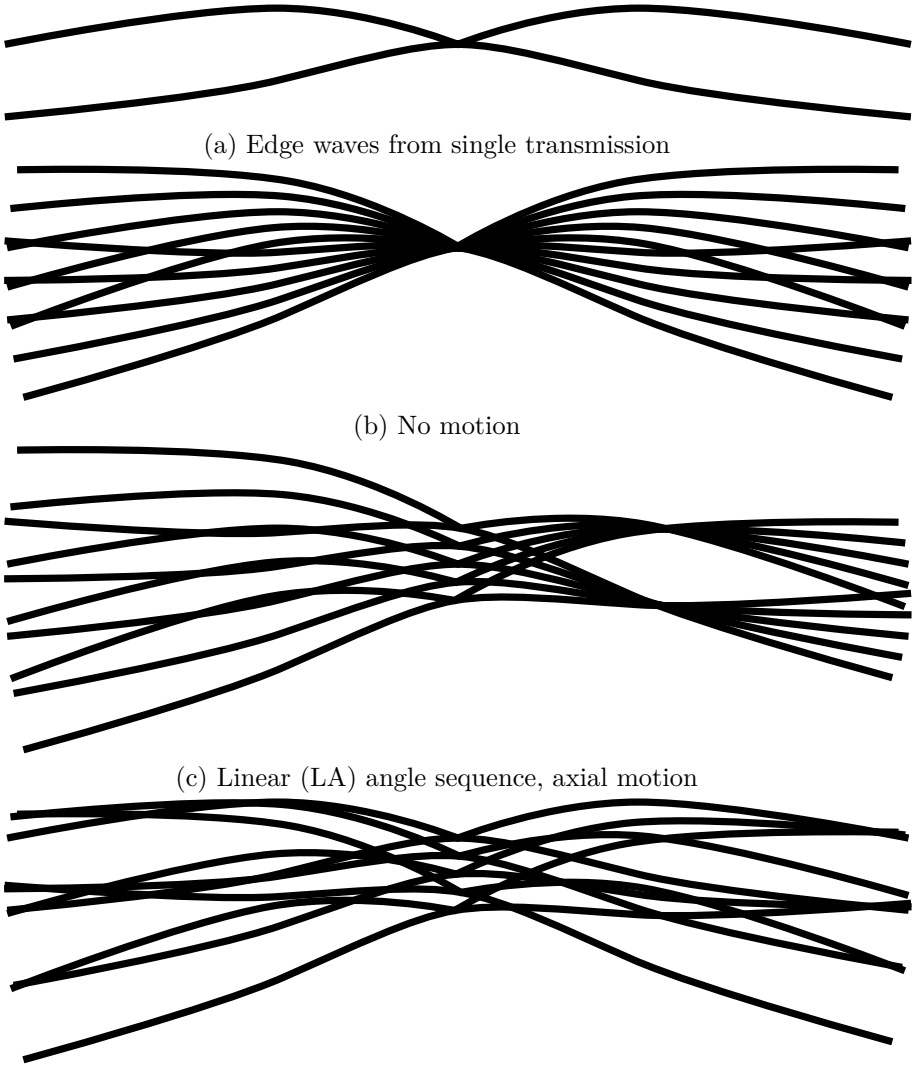

(a) Edge waves from single transmission

(b) No motion

(c) Linear (LA) angle sequence, axial motion

(d) Alternating polarity (AP) angle sequence, axial motion

Figure 5: The individual plane wave transmissions give edge waves. Tilted transmission waves give tilted edge waves. Scatterers moving axially away from the transducer moves the centers of the edge waves downward. (a) Single transmission. (b) Five transmissions for a stationary scatterer. (c) Five transmissions in the LA sequence for a moving scatterer. (d) Five transmissions in the AP sequence for a moving scatterer.

2.11 Motion correction

Motion correction of scatterer motion between successive beam transmissions has been discussed previously for synthetic transmit beams (STB) by Denarie et al. in 2011 [16]. STB is a variant of parallel beamforming proposed by Hergum et al. in 2007 [18]. Parallel beamforming is beamforming of multiple scan lines per transmit beam using broader transmit beams. However, this invokes spatial variance as receive beams are acquired from different portions of the transmit beam and from unaligned transmit and receive beams. STB reduces the artifacts caused by the spatial variance across the image by interpolating the received signal from two neighboring transmit events. A scan line $\overrightarrow{y_\theta}$ in the direction θ is an interpolation between the IQ-demodulated signals $\overrightarrow{x_{n,\theta}}$ and $\overrightarrow{x_{n+1,\theta}}$ from transmits n and n+1, focused in direction θ.

$$\overrightarrow{y_\theta} = \lambda \cdot \overrightarrow{x_{n,\theta}} + (1-\lambda) \cdot \overrightarrow{x_{n+1,\theta}} \tag{22}$$

λ is a parameter dependent on the proximity of the two original receive lines.

To reduce the motion artifacts due to the STB combination of received signal from two transmissions, Denarie et al. [16] proposed phase correction using the cross correlation (section 2.6) of the two overlapping receive lines. The expanded version of 22 is given below.

$$\overrightarrow{y_\theta} = \lambda \cdot e^{-i(1-\lambda)\langle<C_{n,\theta}\rangle} \cdot \overrightarrow{x_{n,\theta}} + (1-\lambda) \cdot e^{-i\lambda\langle<C_{n,\theta}\rangle} \cdot \overrightarrow{x_{n+1,\theta}} \tag{23}$$

$C_{n,\theta}$ is the cross correlation between $\overrightarrow{x_{n,\theta}}$ and $\overrightarrow{x_{n+1,\theta}}$. Velocities higher than $v_c = c \cdot PRF/(4 \cdot f_0)$, where f_0 is the center frequency of the ultrasound pulse cause phase shifts of more than π and cannot be corrected using this technique.

2.11.1 Expanding to coherent plane-wave compounding

As in STB, coherent plane-wave compounding combines receive signals from multiple transmission events. However, the number of plane-wave transmissions can be of the order of 80, all phase shifted relative to each other. A logical expansion of the correction technique proposed in [16] is to take the cross correlation of all received echoes with the echoes from the middle transmitted beam, which will align the phase of all signals for velocities lower than

$$v_N = \frac{v_c}{(N-1)/2} = \frac{c \cdot PRF}{2(N-1)f_0}. \tag{24}$$

This maximum velocity is reduced by half the number of transmit angles compared to the STB version, because the total phase shift from the first to the middle transmitted beam must be taken into consideration.

The cross correlation is calculated for each sample as in (2). To prevent phase correction of clutter, only samples with normalized correlation calculated using (3) above a certain limit should be corrected.

3 Materials and Methods

3.1 Beamforming

All coherent plane-wave beamforming was performed in MATLAB [24] using functions developed at the Department of Circulation and Medical Imaging. The beamforming code had the received signal, acquisition starting time and desired output coordinate axes as input and returned the delayed signal. Linear interpolation was applied to provide correct axial delays and lateral upsampling.

3.2 Angle selection

The coherent plane-wave compounding has been performed using several plane-wave combinations. The tilt angles have been selected according to (15) and (16), but to investigate the effect of using fewer angles, decimated sets of angles and sets with a lower maximum angle have also been investigated. The approximation in (16) gives an error of about 0.15° for the largest angles, which correspond to ca. 1 % of this angle.

For the simulations, a transmit frequency of 6.67 MHz was used, which yields 85 angles separated by 0.338° when a transmit F-number of 2 is desired. The angles were distributed evenly around 0°, making the maximum angle ±14.3°. When using decimated sets of angles, the two largest tilt angles of each polarity were not used to ensure the same maximum angle, and thus F-number, for all decimation factors. This required the number of angles to be on the form $8k+1$, where k is and integer.

For measurements, the transmit frequency was set to 6.60 MHz. (15) and (16) give 83 angles with an angle spacing of 0.344° when requiring an F-number of 2. The maximum angle for this optimal selection was ±14.1°. For acquisitions with decimated angles, up to 81 angles centered around 0° were used.

The number of angles used in the decimated or shortened angle selections are shown in Table 1. The actual maximum angle used varies slightly between simulation and measurements because of the different transmit frequencies, but the F-number is equal to the first decimal. The number of angles is exactly the same.

The first row of Table 1 corresponds to using all angles, which will be referred to as the optimal angle selection. This selection gives imaging characteristics comparable to fixed-focus imaging, cf. section 2.9.1. Rows 2-4 have angle selections with a reduced maximum angle, corresponding to a higher F-number, and were used when the effect of reduced angle selections through decimation or reduced maximum angle was investigated.

All plane-wave images have been beamformed to 512 lateral samples.

Table 1: Angle selection for simulations (freq. 6.67 MHz*) and measurements (freq.* 6.60 MHz*). Maximum angles* 14.3°*,* 13.6°*,* 10.9° *and* 8.2°*, and* 14.1°*,* 13.7°*,* 11.0° *and* 8.2° *used for simulations and measurements, respectively. Decimation factors* 1*,* 2*,* 4 *and* 8 *were employed.*

Maximum angle [°]	No. angles				F-number
Dec. factor	1	2	4	8	
14.3/14.1	85/83	-	-	-	2.0
13.6/13.7	81	41	21	11	2.1
10.9/11.0	65	33	17	9	2.6
8.2/8.2	49	25	13	7	3.5

3.3 Simulations

The simulated results in this report are created using the simulation program Field II [23], which simulates wave fields and received echoes based on a specified phantom, transducer and scan sequence. FieldSim, a set of functions to facilitate the use of Field II, was used. Both Field II and FieldSim are MATLAB-programs, with some external C-code functions. For plane-wave simulations, FieldSim returned the received RF-signal from all channels and for all transmission angles. For fixed-focus simulations, FieldSim returned beamformed IQ-data.

The first returned sample from FieldSim corresponds to the first received reflection from the given phantom. This makes the time of the first returned sample dependent on the position of the closest simulated scatterer. This scatterer will also be impossible to image, because the first samples must be discarded due to interpolation artifacts. The artifacts occur because waves at different angles have different start times due to differences in reflection times, and because beamforming delays may need earlier, non-existing samples. This was solved by placing a single scatterer at a distance 0.3 mm from the transducer at all times. This scatterer was not included in the processed images and should not interfere with signals from deeper lying scatterers.

The transducer specifications in the simulations were chosen to mimic an Ultrasonix L9-4/38, a linear array transducer with 1×128 elements, pitch 304 µm and elevation focus depth 19 mm. The center transmit frequency was 6.67 MHz. When doing plane-wave simulations, the lateral focus was set to 5.0 m, to produce approximately plane waves. For the simulation of focused waves, the lateral focus was set to the desired focal depth at transmission, and dynamic focusing was performed on receive. Both fixed-focus images and plane-wave images were simulated with Hamming receive apodization. Both transmit and receive F-numbers for the conventionally focused simulations and receive F-number for the plane-wave simulations were 2, while the transmit F-number for the coherent plane-wave compound varied according to maximum tilt angle used, as shown in Table 1.

The lateral resolution was measured from simulations of single point scatterers, while the contrast was measured using a simulated cyst phantom.

3.3.1 Simulated movement

For simulation of moving objects, the position of a simulated point scatterer was changed between waves to indicate the movement of the scatterer. For a scatterer velocity of 1.0 cm/s, using a PRF of 12 kHz, the movement between angles was 0.83 µm per plane wave, and up to almost 68 µm for a full frame. The simulated velocities were 1.0, 3.0, 5.0 and 10.0 cm/s axially, away from the transducer, and 5.0 and 10.0 cm/s laterally.

Moving cysts were simulated by moving all the surrounding scatterers downward, away from the transducer. The simulated velocities were 5.0 and 10.0 cm/s.

The angle sequences used were the linear (LA) and alternating polarity (AP) sequences, which are explained in section 2.10.1.

3.4 Measurements

The transducer used for all measurements was an Ultrasonix L9-4/38, transmitting with a center frequency of 6.60 MHz for both imaging techniques. The plane wave acquisitions were controlled by MATLAB scripts and recorded using a digital acquisition system, DAQ, while the program Sonix 6.0.0 included on the Ultrasonix SonixMDP-scanner was used to transmit and record the fixed-focus waves. F-numbers on both transmit and receive were 2.0, except for the focused waves at maximum depth 47 mm, where the minimum obtainable F-number on receive was 2.4, and the transmit F-number of the plane-wave compounds, which ranged from 2.0 to 3.5 (Table 1). The PRF for the plane-wave compound was 12 kHz for *in vitro* measurements and 16 kHz for *in vivo* measurements, leading to frame rates from 140 to 1500 fps, depending on the number of angles used. The fixed-focused measurements had a frame rate of 55 fps and 256 transmit beams were used.

3.4.1 *In vitro* measurements

For resolution calculations, recordings of a string of diameter 0.2 mm in a water tank were made. The string was positioned at 20, 30, 40 and 50 mm (47 mm for focused waves) depth. To prevent reverberations from the tank walls, the PRF was reduced to 4000 Hz for the plane wave technique and to 4900 Hz for the focused waves during water tank acquisitions. This ensured no apparent reverberations from the tank within the imaged area. Fixed-focus images were acquired for all combinations of focal depths and string depths. Plane-wave images were beamformed using the selections of angles presented in Table 1.

For contrast calculations, the Near Field Ultrasound Phantom 050 from CIRS (Norfolk, Virginia) was used to acquire images of a non-echoic cyst at 10 mm depth using conventional focal depths 10, 20, 30 and 40 mm and plane-wave tilt angles from Table 1.

3.4.2 *In vivo* measurements

Recordings of the parasternal long axis view of a young rat's left ventricle were made to investigate the effect of motion *in vivo*. The imaged rat had a heart rate of 450 bpm = 7.5 bps, enabling 26 to 194 frames per heart cycle. Wall velocities in a rat heart are of the order of 5 cm/s [25].

Acquisitions were made using all decimation factors, and using the largest available maximum angle for each decimation factor (14.1° for dec. 1 and 13.7° for dec. 2-8). Both the LA and the AP sequence were used.

The available transducer was not ideal for rat imaging, as the small size and detailed structures of the rat anatomy favors a frequency of about twice the center frequency of the Ultrasonix L9-4/38 transducer.

3.5 Correction of motion artifacts

In order to correct for the phase differences introduced by moving scatterers, cross-correlation correction (CCC) was attempted (section 2.11.1). The cross correlation between the received echoes for the middle tilt angle and the received echoes for all other tilt angles was computed using (2), summing over $2m + 1 = 31$ axial samples corresponding to 2.5 pulse lengths. The normalized correlation limit was set to 0.97 for simulations and 0.90 for measurements.

3.6 Evaluation of image quality

Several measurements were used to quantify image quality. This report presents numbers on contrast and resolution, with the aid of calculated beam profiles.

3.6.1 Beam profile calculation

Lateral and axial beam profiles were calculated by adding the intensity values in the orthogonal direction, by summing over z and x, respectively, as shown in (25a) and (25b).

$$p_x(x) = 10 \cdot \log_{10} \frac{\sqrt{\sum_z I(z,x)}}{\max\left(\sqrt{\sum_z I(z,x)}\right)} \tag{25a}$$

$$p_z(z) = 10 \cdot \log_{10} \frac{\sqrt{\sum_x I(z,x)}}{\max\left(\sqrt{\sum_x I(z,x)}\right)} \tag{25b}$$

I is the signal intensity of the image, the square of the amplitude envelope.

3.6.2 Resolution

The resolution of an image is the minimum distance between two objects that enables them to be imaged as two separate objects. A much used measure of the resolution

is the two-sided $-10\,\mathrm{dB}$ width of the point spread function, represented by beam profiles in this report. Axial resolution are measured using the $-20\,\mathrm{dB}$ width.

Where more than one peak in the beam profile rises above the resolution limit, the distance from the first to the last point above the limit is reported.

An image with a good resolution has a low minimum distance compared to an image with worse resolution. In this report, an improved resolution refers to a shorter distance between separable points.

3.6.3 Contrast

Contrast is the ability to discern areas with different acoustical impedances. Optimal contrast would be achieved if each point in the object would map perfectly to a pixel in the image. Because of imperfect imaging methods, some of the energy scattered from a point will be spread out across the image, reducing the contrast. All contrast results presented here have been calculated as the energy level inside a 5 mm-radius non-echoic cyst relative to the energy level from scatterers surrounding the cyst, as shown in (26).

$$\text{contrast} = 10 \cdot \log_{10} \frac{\bar{I}_{in}}{\bar{I}_{out}} \tag{26}$$

All points inside a radius of 3.5 mm have been defined as inside the cyst, while points outside a radius of 5.5 mm have been used to calculate the energy level of the scatterers.

A good contrast means little clutter inside the cyst, meaning a low mean energy level compared to the energy level outside of the cyst. In decibel, this corresponds to a large, negative value. In the following, an improved contrast means an increase in absolute value of the contrast measure.

3.7 Summary of presented results

Table 2 presents an overview of the simulations and measurements that have been performed.

Table 2: Simulations and measurements

How	What
Simulations	Point scatterer and cyst, stationary and moving
In vitro measurements	Point scatterer (string) and cyst phantom, stationary
In vitro measurements	Rat heart (left ventricle)

4 Results

4.1 Stationary objects

The resolution and contrast from simulations and *in vitro* measurements of point scatterers and cysts employing the coherent plane-wave compounding technique and conventional fixed-focus waves were measured as described in sections 3.6.2 and 3.6.3. All the numerical results are given in appendix A.

4.1.1 Simulations

Contrast and resolution of point scatterers from simulations with focused waves and with coherently compounded plane waves were reported in [26]. It later turned out that the parameters used in these simulations did not match the parameters of the Ultrasonix L9-4/38. The simulated acquisitions in the present report were generated with correct kerf, element height and elevation focus to match those of the real transducer. The F-number and transmit frequency have also been adjusted, Hamming receive apodization was included, and an updated version of the beamforming code (section 3.1) has been used. In addition, different methods for contrast and resolution calculation have been implemented. The results, however, showed similar trends.

Results for the -10 dB lateral resolution measured from beam profiles of point scatterers at different depths are presented in Fig. 6. The results are shown for simulations using the optimal coherent plane wave compound, using the angle selection of the first row of Table 1, together with results from simulations of conventionally focused waves focused at ranges 20, 30, 40 and 50 mm.

For the coherent plane-wave compound, the measured lateral resolution ranged from 0.67 mm at 20 mm depth to 0.81 mm at 50 mm depth. The multifocal results, ie. using the focal depth corresponding to the current point depth, ranged from 0.70 mm to 0.77 mm for the same depths. The resolution achieved for points away from the transmit focal depth of the fixed-focus waves was worse, reaching values of 1.1 mm only 5 mm away from the focal depth, and a maximum value of 1.56 mm.

The contrast was only evaluated for a cyst depth of 30 mm. It was found to be -39.1 dB for the simulated plane-wave compound, while the contrast achieved with conventionally focused waves focusing at the middle of the cyst was -36.1 dB. Results found using other focal depths ranged from -35.7 to -38.8 dB.

Some results were calculated without the approximation in (16), but the results were identical to those achieved using approximated angles.

Reduced angle selection The resolution achieved using the coherent plane-wave compound for a varying decimation factors is shown in Fig. 7 as a function of maximum angle, using the angle selections from rows 2-4 in Table 1. Referring to (17), the maximum angles utilized here of 8.2°, 10.9° and 13.6°, correspond to F-numbers 3.5, 2.6 and 2.1. For F-number 2.1 (13.6°), the resolution was 0.69 to 0.72 mm, achieving the best resolution using the largest decimation factor, corresponding to fewest angles and largest angle spacing. For F-number 3.5 (8.2°), the resolution was found to be in the range from 0.92 to 0.98 mm, again with the best resolution using the largest decimation factor. The improvement in resolution by extending the

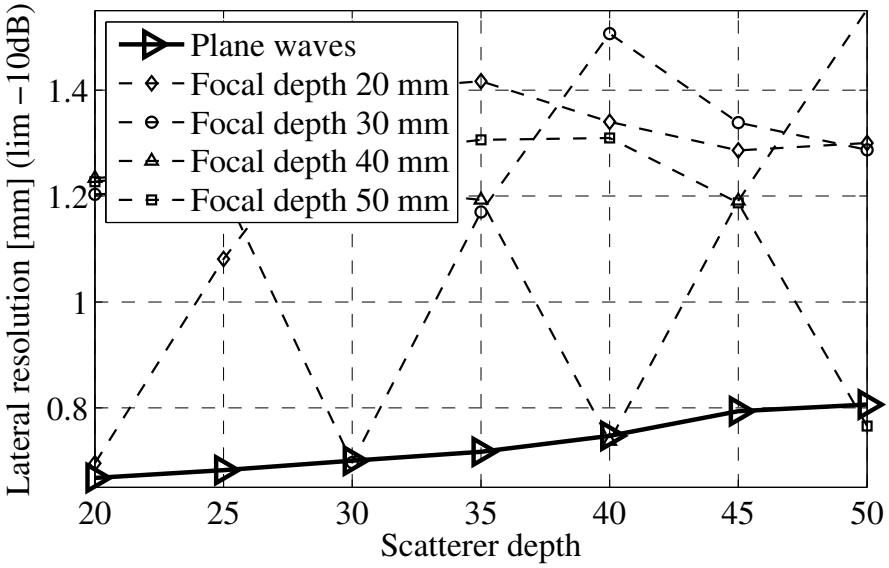

Figure 6: Lateral resolution calculated using −10 dB *limit for simulated stationary point scatterer placed at depths* 20, 30, 40 *and* 50 mm *for focused waves focusing at* 20, 30, 40 *and* 50 mm *and for the optimal plane-wave combination (row 1 in Table 1).*

maximum angle from 8.2° to 13.6° with no angle decimation is thus 0.26 mm, while the improvement of changing the decimation factor does not exceed 0.06 mm for any given maximum angle.

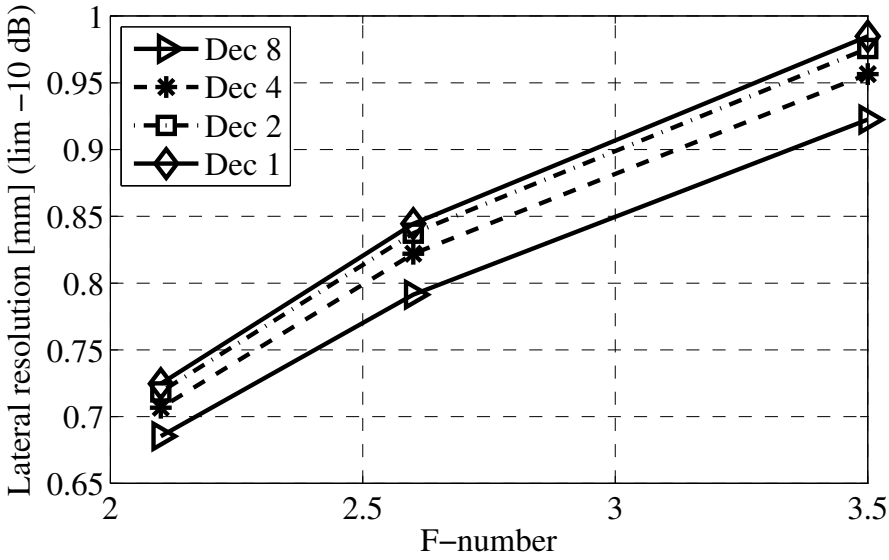

Figure 7: −10 dB *lateral resolution for simulated stationary point scatterer placed at depth* 30 mm *for several plane-wave combinations of decimation factors* 1 - 8 *and maximum angles* 8.2°, 10.9° *and* 13.6° *($F_\#$* 3.5, 2.6 *and* 2.1*) as a function of F-number (rows 2-4 in Table 1).*

The contrast calculated using a cyst at 30 mm depth is presented in Fig. 8 for maximum angles 8.2°, 10.9° and 13.6° ($F_{\#}$ 3.5, 2.6 and 2.1) as a function of decimation factor. The best resolution of −40.4 dB was achieved using decimation factor 1 and the lowest maximum angle (8.2°, $F_{\#}$ 3.5). The loss in expanding the maximum angle to 13.6° was 1.3 dB, while the loss in doubling the angle spacing, using a decimation factor of 2, was 11.4 dB for the highest maximum angle ($F_{\#}$ 2.1) and 7.2 dB for the lowest maximum angle ($F_{\#}$ 3.5). The calculated contrast loss by increasing the angle spacing from decimation factor 2 to decimation factor 8 was 4.4 to 7.0 dB, depending on the maximum angle used. A low maximum angle gave the best contrast for all decimation factors.

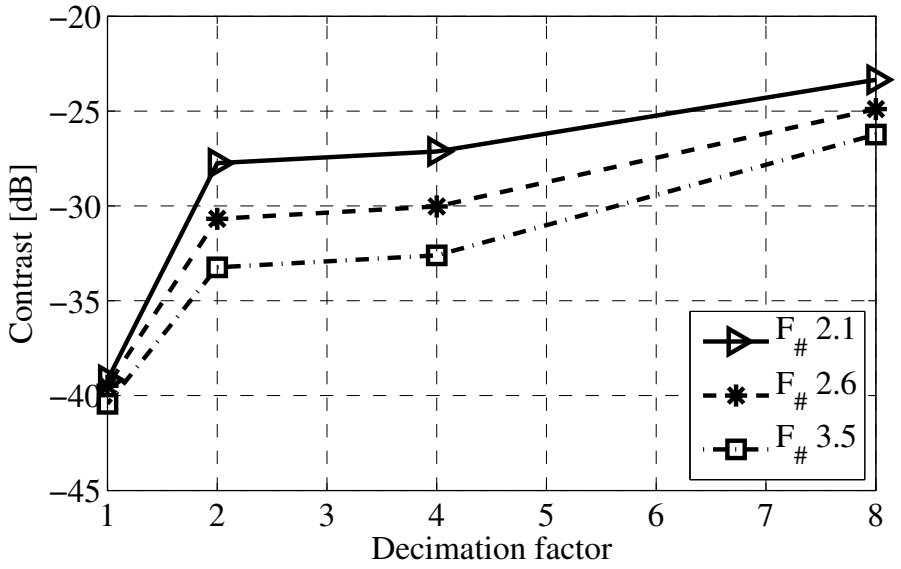

Figure 8: Contrast for simulated stationary cyst placed at depth 30 mm *for several plane-wave combinations of decimation factors* 1 - 8 *and maximum angles* 8.2°*,* 10.9° *and* 13.6° *($F_{\#}$* 3.5*,* 2.6 *and* 2.1*) as a function of decimation factor (rows 2-4 in Table 1).*

Fig. 9 shows lateral beam profiles for a point scatterer simulated using several decimation factors and maximum angle 13.6°, corresponding to an F-number of 2.1. No apodization was applied in order to study the side lobes present for higher decimation factors. The distance from the scatterer position to the first side lobes is $d_8 = 5.4 \pm 0.1$ mm for decimation factor 8 and $d_4 = 11.9 \pm 0.1$ mm for decimation factor 4. The second side lobe for decimation factor 8 coincide with the first side lobe for decimation factor 4. This gives values of $\frac{d}{L}$ of 0.31 and 0.14 for decimation factors 4 and 8, respectively.

4.1.2 *In vitro* measurements

The simulated −10 dB lateral resolution has been validated *in vitro* using acquisitions of a string in a water tank. The results are presented in Fig. 10 for the optimal plane-wave combination using 83 angles (first row of Table 1) and conventionally

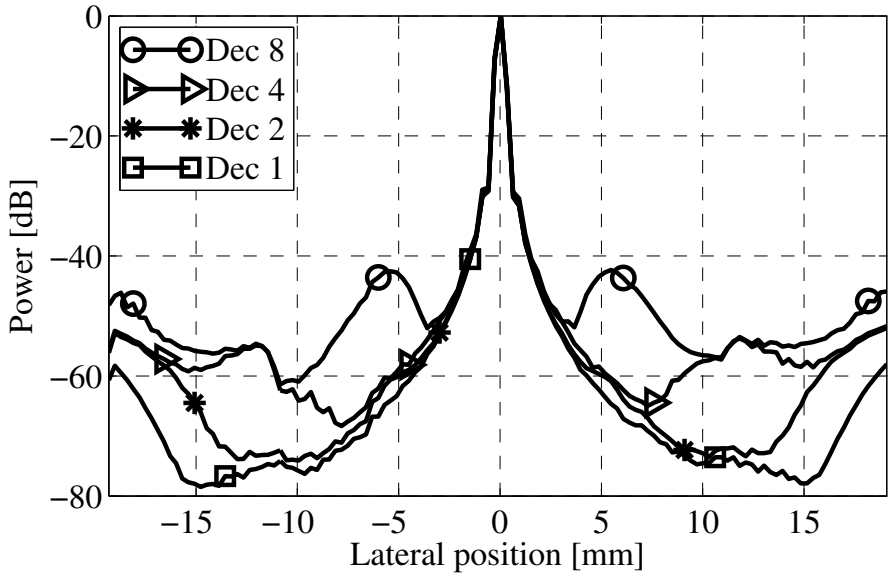

Figure 9: Beam profiles of simulated stationary point scatterer at depth 30 mm. *Maximum angle* 13.6° *($F_\#$* 2.1*) for all profiles, decimation factors* 1, 2, 4 *and* 8 *(row 2 in Table 1). No apodization used.*

focused waves with varying focal depth as a function of scatterer depths. The multifocal combination has been highlighted for better comparison with the optimal plane-wave compound.

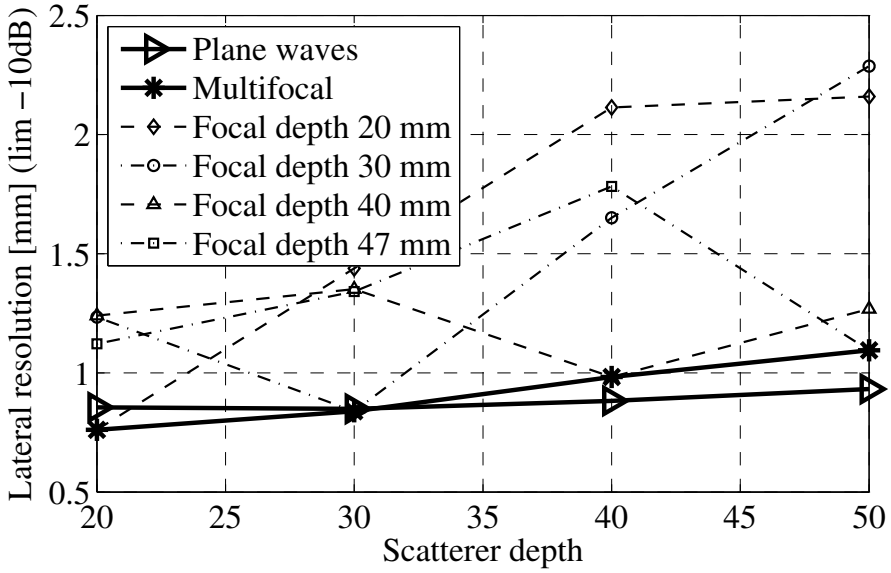

Figure 10: −10 dB *lateral resolution for* in vitro *point scatterer (string) placed at depths* 20, 30, 40 *and* 47 mm*, for focused waves focusing at* 20, 30, 40 *and* 47 mm *and for the optimal plane-wave combination (row 1 in Table 1). The multifocal results have been highlighted.*

The lateral resolution obtained by the coherent plane-wave compound was 0.85-0.93 mm, while the results at the focal depths of the fixed-focus waves ranged from 0.76 to 1.10 mm. The best resolution achieved by conventionally focused waves away from the transmit focal depth was 1.12 mm, but most off-focus resolutions exceeded 1.2 mm, some reaching lateral resolutions of 2.3 mm.

The cyst used for contrast measurements was at a depth of 10 mm. The contrast of the coherent plane-wave compound was −26.8 dB, while the contrast using waves focused at the cyst depth was calculated to be slightly better at −28.7 dB. The contrast results for transmit focal depths of 20 to 40 mm ranged from −25.5 to −18.4 dB, which was a loss of 3.2-10.3 dB compared to the optimally focused fixed-focus images, and 1.3-8.4 dB compared to the plane-wave compound.

Reduced angle selection As for the simulated images, the effect of angle reduction by lowering the maximum angle or increasing the decimation factor was investigated, and the results for scatterer depth 30 mm are displayed in Figs. 11 and 12. The maximum angles of 8.2°, 11.0° and 13.7° yield F-numbers of 3.5, 2.6 and 2.1, according to (17).

The lateral resolution of *in vitro* measurements behaved exactly as the simulated counterparts when the angle selection was varied. The resolution for maximum angle 13.7° ($F_\#$ 2.1) was within the range 0.83-0.86 mm for all decimation factors. The best resolution was found using decimation factor 8 with worsening results for lower decimation factors. The same is seen for maximum angles of 8.2° and 11.0° ($F_\#$ 3.5 and 2.6), where the resolution varied from 1.05 to 1.11 mm and from 0.91 to 0.97 mm, respectively. The effect on the lateral resolution of changing the maximum angle is much greater than the effect of changing decimation factor.

The contrast was in the range of −24.0 to −26.7 dB for all maximum angles and for decimation factors 1 and 2, while decimation factors 4 and 8 gave contrast results between −10.4 and −14.1 dB. The contrast for the highest maximum angle was better than for lower maximum angles for all decimation factors, while the contrast generally worsened with increasing decimation factors, as seen in Fig. 12.

4.2 Moving objects

4.2.1 Lateral resolution

Some lateral resolutions for simulated moving point scatterers have been listed in Table A.9 for axial and lateral velocities from 0 to 10 cm/s, which equals up to 8.33 µm displacement per transmitted wave. Only decimation factors 1, 2 and 4 and maximum angles 8.2° and 13.6° ($F_\#$ 3.5 and 2.1) have been studied. The effect on lateral resolution of lateral motion is smaller than the effect of axial motion. The best lateral resolution found for a stationary scatterer of 0.67 mm differ by no more than 0.11 mm from the worst resolution found for a scatterer with lateral velocity 5.0 cm/s for maximum angle 13.7° ($F_\#$ 2.1). For this maximum angle, a lateral velocity of 10.0 cm/s gives a maximum lateral resolution of 1.16 mm, found using decimation factor 1. For maximum angle 8.2° ($F_\#$ 3.5), the best and worst

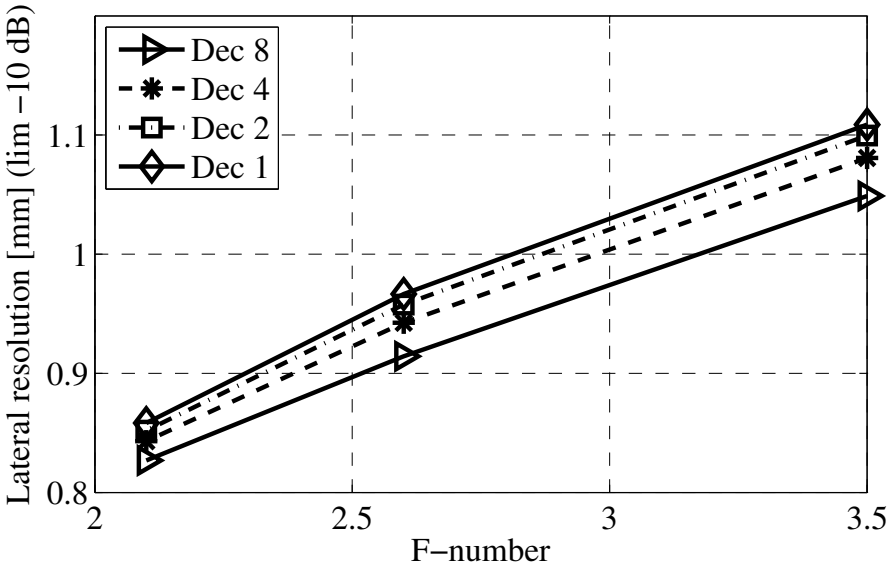

Figure 11: $-10\,\mathrm{dB}$ *resolution for* in vitro *point scatterer (string) placed at depth* $30\,\mathrm{mm}$ *for several plane-wave combinations of decimation factors* 1 - 8 *and maximum angles* $8.2°$, $11.0°$ *and* $13.7°$ *(*$F_\#$ 3.5, 2.6 *and* 2.1*) as a function of maximum angle (rows 2-4 in Table 1).*

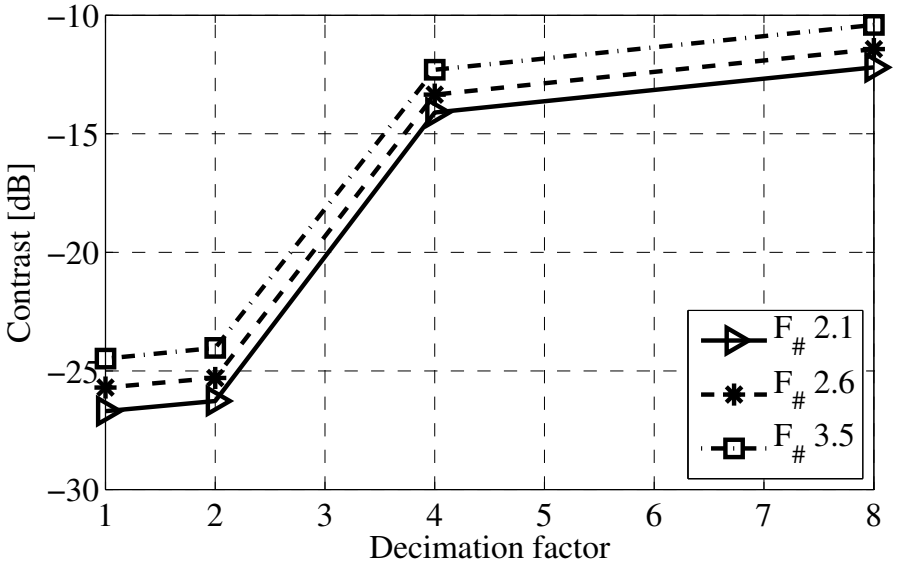

Figure 12: Contrast for in vitro *point scatterer (string) placed at depth* $30\,\mathrm{mm}$ *for several plane-wave combinations of decimation factors* 1 - 8 *and maximum angles* $8.2°$, $11.0°$ *and* $13.7°$ *(*$F_\#$ 3.5, 2.6 *and* 2.1*) as a function of decimation factor (rows 2-4 in Table 1).*

resolutions were 0.91 and 1.01 mm, respectively, for all scatterer velocities up to 10.0 cm/s.

The resolution for axial velocities has been plotted in Fig. 13. There is no general pattern in the resolution as a function of velocity, as this is dependent on many factors. The lateral resolution achieved using a certain selection of tilt angles is different for each angle sequence and each velocity. For the LA sequence, a decimation factor of 4 gives the best resolution at high velocities, while the same angle selections gives the worst resolution at this velocity for the AP sequence.

In Fig. 14, beam profiles from scatterers simulated using sequences LA and AP are shown for axial velocities 3.0, 5.0 and 10.0 cm/s. Referring to Fig. 14e, the LA sequence gives rise to a distinct peak 3 mm to the right of the main lobe, while the AP sequence has two peaks at about 5 mm to either side of the main lobe. At half the scatterer velocity in Fig. 14c, the distance to the peaks is approximately halved. At a scatterer velocity of 3.0 cm/s, the peaks add to the main lobe, increasing the amplitude for the LA sequence in such a way that the proper point position at lateral position 0 mm no longer has the highest amplitude. For the AP sequence, the two peaks increase the width of the main lobe which results in a poor −10 dB lateral resolution, as seen in Fig. 13.

Using a certain angle sequence, a certain velocity may lead to the combination of main peak and side peak. This degrades the lateral resolution for this velocity, while the resolution for the same set of angles may improve at a larger scatterer velocity when the side peak has separated from the main peak. As the peak at a given set of angles and velocity is further away for the AP sequence than for the LA sequence, the velocity which gives the poorest resolution due to peak combination is generally lower for the AP sequence than for the LA sequence. At velocities lower than the critical velocity for peak combination, most of the energy is collected within the main lobe and the resolution degradation is minimal.

The worst lateral resolution of the motion simulations was 1.73 mm, which occurred at an axial velocity of 3.0 cm/s for decimation factor 1 and maximum angle 8.2° ($F_{\#}$ 3.5) in the AP sequence. At higher velocities, the lateral resolution for this set of angles improved again. For an axial velocity of 10.0 cm/s both the worst and the best resolution of 1.56 mm and 0.89 mm were achieved using decimation factor 4 and a maximum angle of 8.2° ($F_{\#}$ 3.5), applying angle sequences AP and LA, respectively.

The clutter level of the sequences is the same, about 20 dB and 30 dB higher for velocities 3.0 cm/s and 10.0 cm/s, respectively, than for the stationary scatterer.

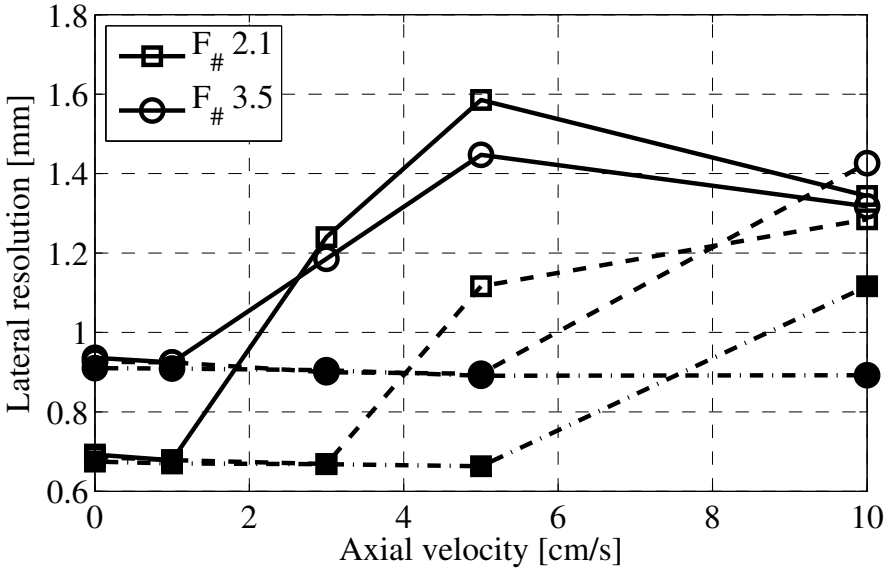

(a) LA sequence

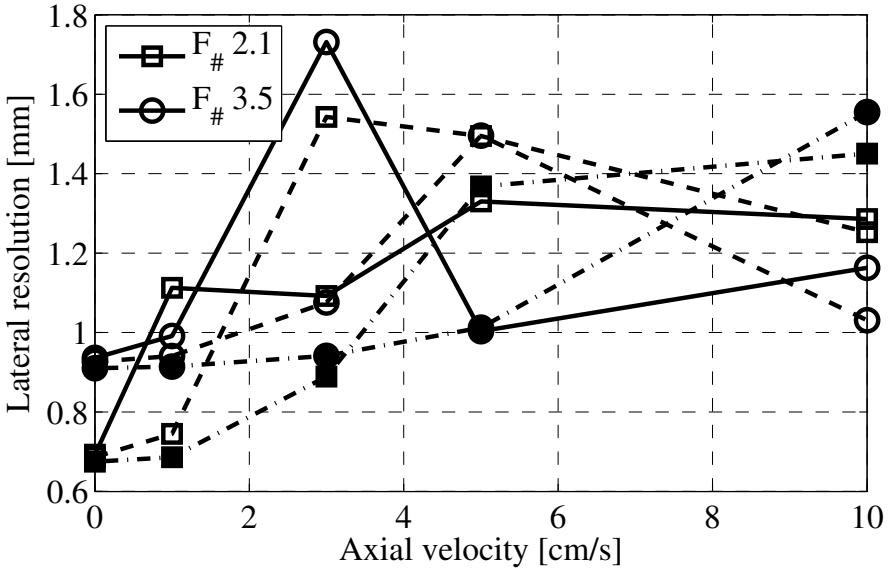

(b) AP sequence

Figure 13: $-10\,\mathrm{dB}$ *lateral resolution for simulated point scatterer as a function of axial velocity using angle selections of decimation factor 1 (solid), 2 (dashed) and 4 (dash-dotted with filled markers) for maximum angles* $13.6°$ *and* $8.2°$ *(*$F_\#$ 2.1 *and* 3.5*) for the (a) LA sequence and (b) AP sequence.*

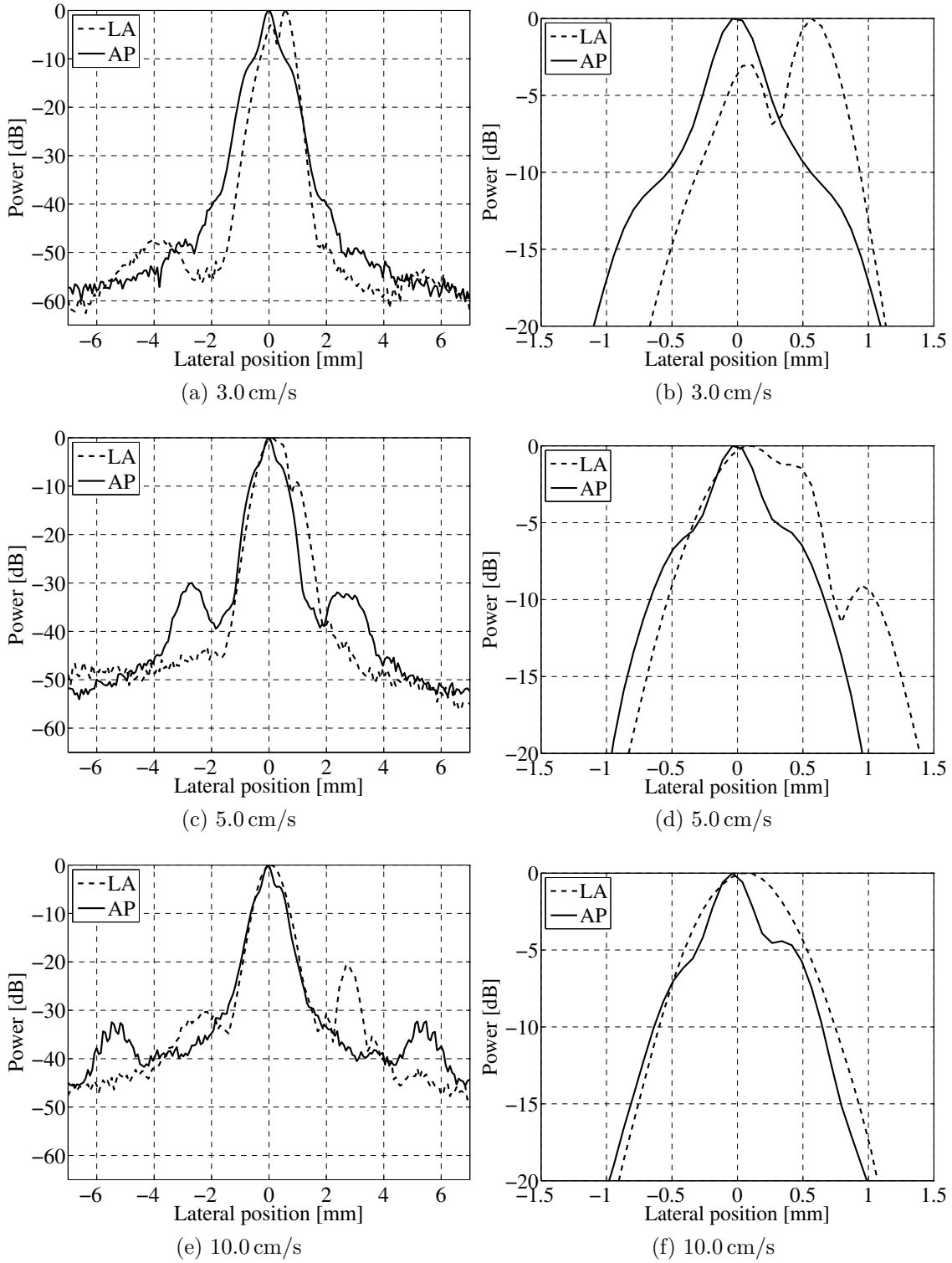

(a) 3.0 cm/s (b) 3.0 cm/s

(c) 5.0 cm/s (d) 5.0 cm/s

(e) 10.0 cm/s (f) 10.0 cm/s

Figure 14: Lateral beam profiles for simulated point scatterer moving at (a) 3.0*, (c)* 5.0 *and (e)* 10.0 cm/s *axially, using LA and AP. Decimation factor* 1 *and maximum angle* 13.6° *($F_\#$* 2.1*) has been used. Right panels show enlargement of central peak.*

4.2.2 Axial resolution

The −20 dB axial resolution is given in Table A.10 for some decimation factors, maximum angles, sequences and velocities. The values for the axial resolution increase with axial motion, but lateral motion does not degrade the resolution by more than 0.01 mm for any angle/velocity combination. Axial resolutions for axial velocities are shown in Fig. 15. The resolution is generally better for larger decimation factors, which means fewer angles, but for higher velocities, a significantly increased resolution of about 5 mm is seen.

The impact of axial motion is illustrated in Fig. 16, where axial beam profiles for decimation factors 1 and 2, maximum angle 13.6° ($F_{\#}$ 2.1) and the LA and AP sequences are shown for axial velocities 3.0, 5.0 and 10.0 cm/s. For both angle sequences, the motion gives two separate peaks at the position of the scatterer when the first and last plane waves are transmitted. Hence, a larger decimation factor, which means fewer angles, ensures a shorter distance between the peaks, as seen in Figs. 16b, d and f.

The range side lobe some millimeters below the point scatterer has a higher intensity for larger velocities, and for larger decimation factors it is the source of the very poor resolution at higher velocities, because side lobe intensities are less than 20 dB below the maximum, as seen in Figs 16c and e. For low velocities, the AP sequence seems to provide less cancellation, and thus more signal, in this area than the LA sequence, cf. Figs. 16a and c. This can also be seen in Fig. 15, as lower velocities and decimation factors result in such a poor resolution for the AP sequence than for the LA sequence.

4.2.3 Point spread function

The point spread function, here represented by an image of the point, is presented in Fig. 17. Although both the LA and AP sequences introduce similar peaks in the axial beam profile, the appearance of a point scatterer is quite different, as seen in Figs. 17a and b. The single high intensity side peak from the LA lateral beam profile (Fig. 14) is really two peaks on the right side, while the two symmetric lower intensity peaks from the AP beam profile are four peaks, two on both sides of the scatterer, all visible in the figure. While the LA sequence images the point as two skew lines at the top and bottom of the point, the AP sequence has more signal between straighter edge lines.

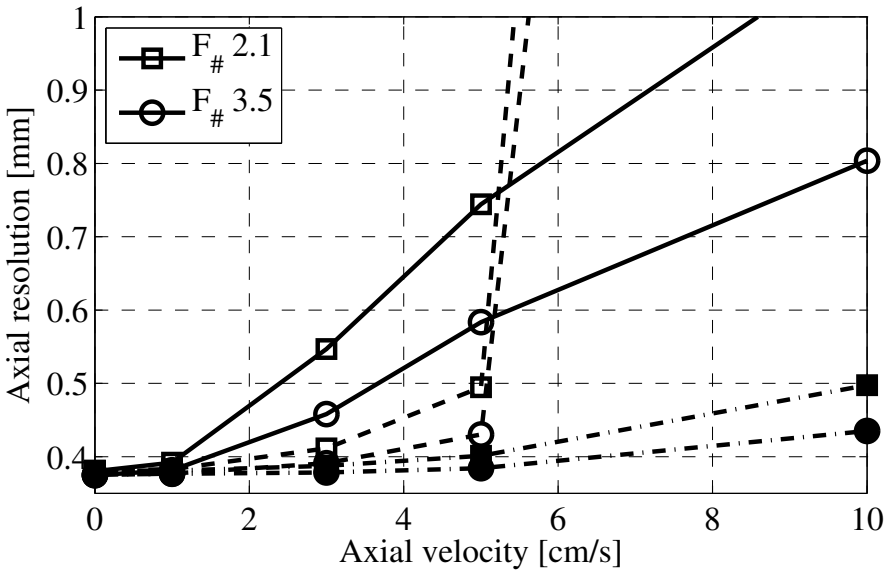

(a) LA sequence

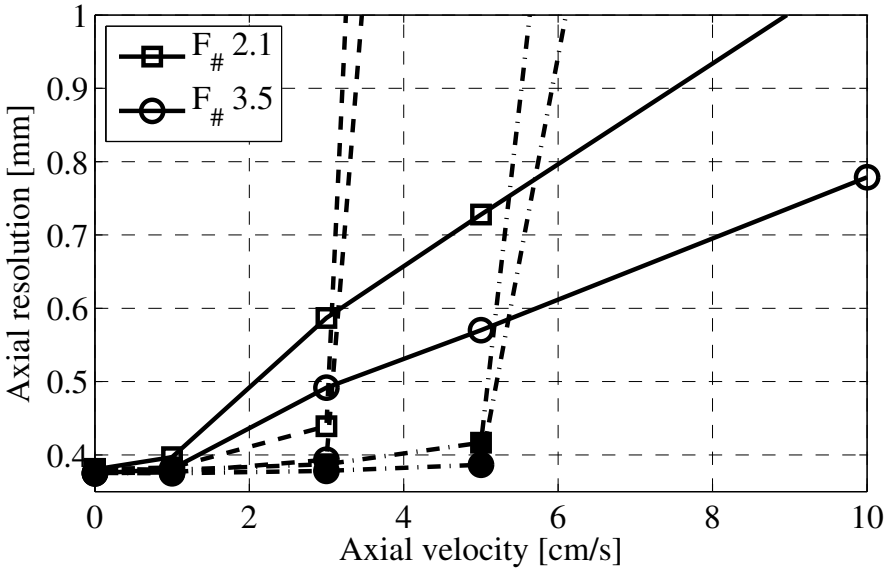

(b) AP sequence

Figure 15: $-20\,\mathrm{dB}$ *axial resolution for simulated point scatterer as a function of axial velocity using angle selections of decimation factor 1 (solid), 2 (dashed) and 4 (dash-dotted with filled markers) for maximum angles* $13.6°$ *and* $8.2°$ *(*$F_\#$ 2.1 *and* 3.5*) for the (a) LA sequence and (b) AP sequence.*

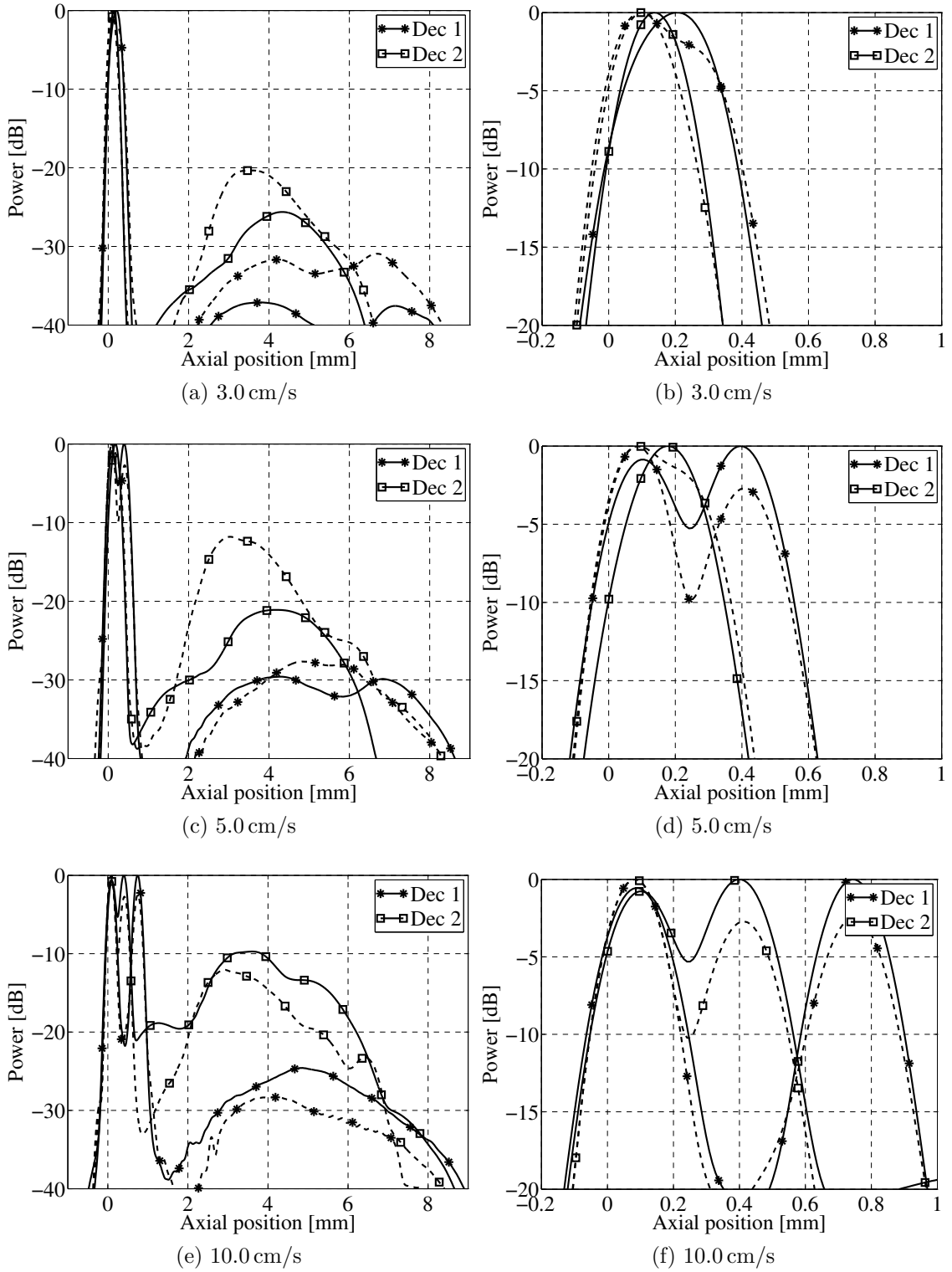

(a) 3.0 cm/s (b) 3.0 cm/s

(c) 5.0 cm/s (d) 5.0 cm/s

(e) 10.0 cm/s (f) 10.0 cm/s

Figure 16: Axial beam profiles for simulated point scatterer moving at (a) 3.0*, (c)* 5.0 *and (e)* 10.0 cm/s *axially, using LA (solid lines) and AP (dashed lines). Decimation factors 1 and 2 and maximum angle* 13.6° *($F_\#$ 2.1) has been used. Right panels show enlargement of main peak.*

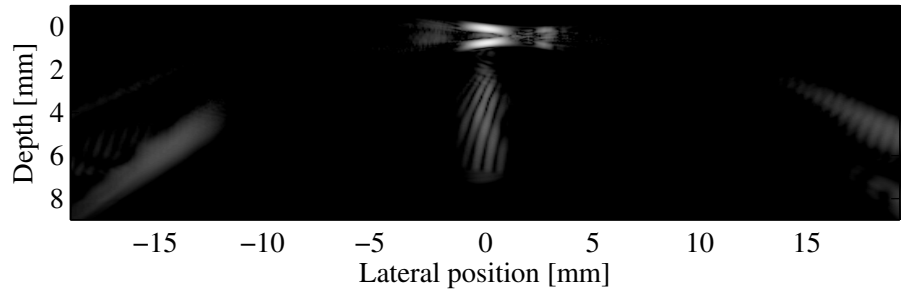

(a) LA

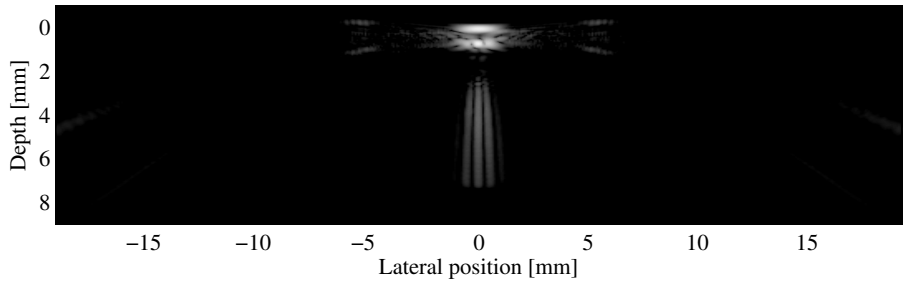

(b) AP

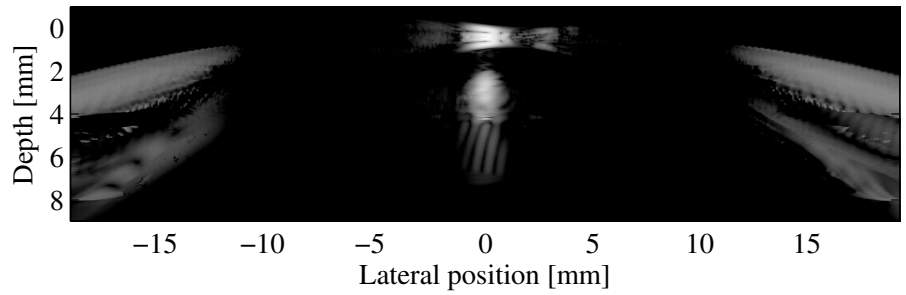

(c) LA CCC

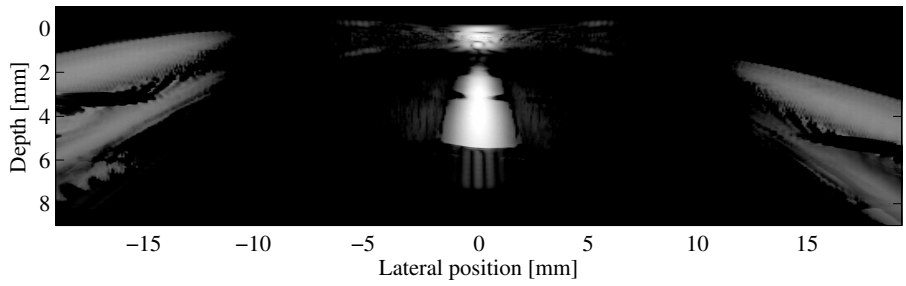

(d) AP CCC

Figure 17: Image of point scatterer moving at an axial velocity of $10\,\mathrm{cm/s}$ *simulated with angle sequences LA (a),(c) and AP (b), (d). Dynamic range* $50\,\mathrm{dB}$*. (c) and (d) have been corrected using CCC. Decimation factor 1 and maximum angle* $13.6°$ *($F_\#$ 2.1) has been used.*

4.2.4 Contrast

The degradation of contrast due to axial motion has been calculated on simulated cysts as described in section 3.3.1. The results are shown in Fig. 18 for sequences LA and AP, and numerical results can be found in Table A.11. The two sequences give similar results for low velocities, with a maximum contrast difference at a velocity of 5.0 cm/s of 0.7 dB. At a velocity of 10.0 cm/s, a decimation factor of 1 or 4 gives a maximum difference of 1.0 dB in favor of the LA sequence, while a decimation factor of 2 yields a contrasts which is up to 8.1 dB better using the AP sequence than using the LA sequence.

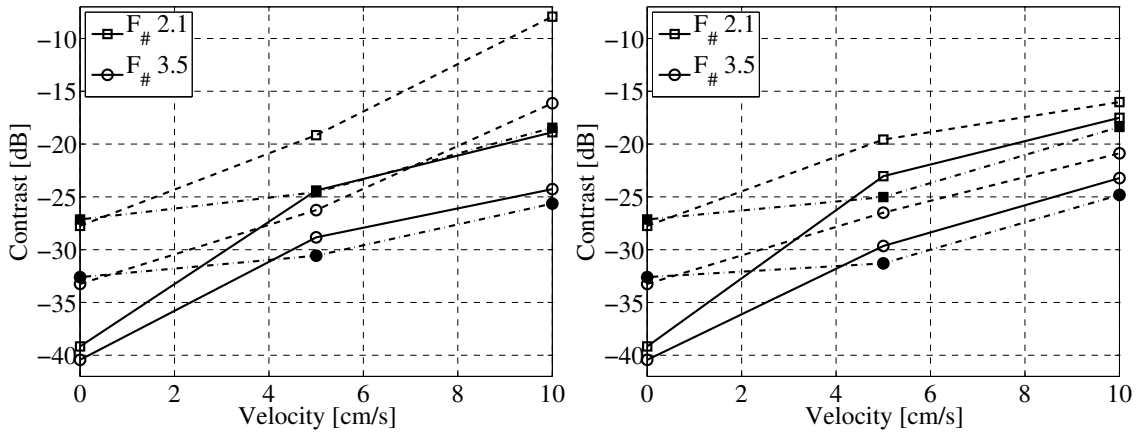

(a) LA (b) AP

Figure 18: Contrast of simulated moving scatterers surrounding a non-echoic cyst for sequences (a) LA and (b) AP for decimation factors 1 *(solid lines),* 2 *(dashed line) and* 4 *(dash-dotted with filled markers) for maximum angles* 13.6° *and* 8.2° *($F_\#$* 2.1 *and* 3.5*) as a function of velocity.*

Images of the simulated cysts are shown in Fig. 19. The cyst imaged using decimation factor of 2, maximum angle 13.6° ($F_\#$ 2.1) using the LA sequence (Fig. 19c) has so much clutter in the upper part of the cyst that the border between the cyst and the surrounding scatterers is vague. This cyst is the reason for the significant contrast difference between the LA and AP sequences for decimation factor 1. There is little difference between the cysts from simulations with decimation factors 1 and 4, and decimation factor 2 for the AP sequence.

The total contrast loss for a velocity of 5.0 cm/s compared to a stationary cyst is ∼16 dB, ∼8 dB and ∼2 dB for decimation factors of 1, 2 4, respectively.

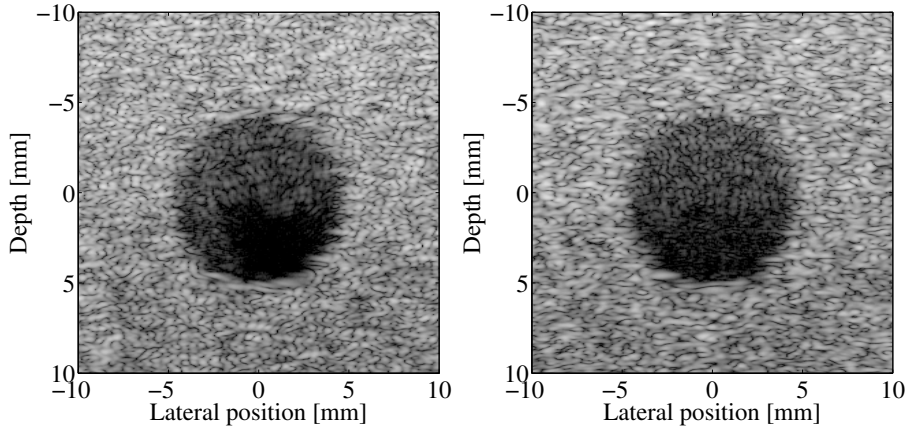

(a) LA, dec 1 (b) AP, dec 1

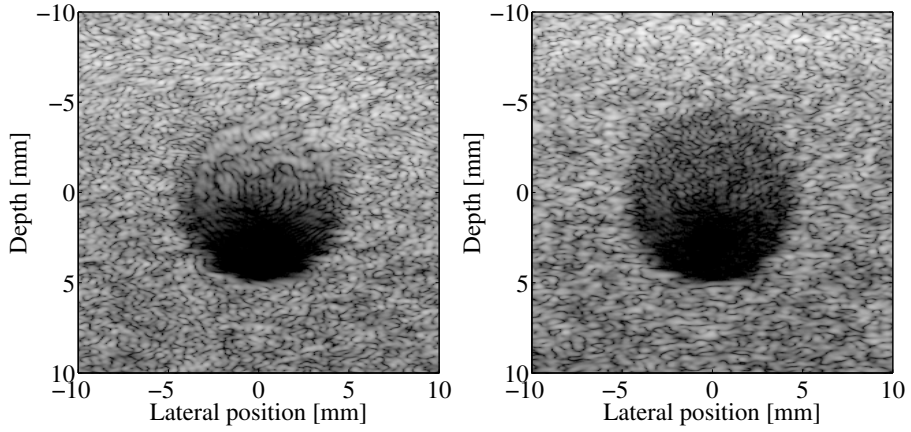

(c) LA, dec 2 (d) AP, dec 2

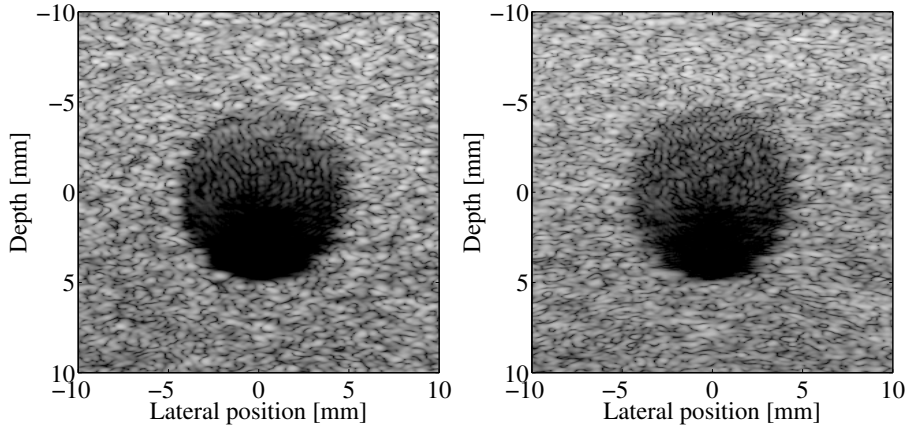

(e) LA, dec 4 (f) AP, dec 4

Figure 19: Simulated cyst images for scatterers surrounding non-echoic cyst moving at 10.0 cm/s *axially. Maximum angle* 13.6° *($F_\#$* 2.1*) has been used. Decimation factors* 1, 2 *and* 4 *and both the LA and AP sequence have been used. Dynamic range* 50 dB. *The gain has been adjusted for better comparison.*

4.2.5 Motion correction

The CCC technique (section 3.5) was attempted to improve the image quality of simulated moving point scatterers. Only decimation factors 1 and 2 and maximum angles 8.2° and 13.6° ($F_{\#}$ 3.5 and 2.1) were studied. Numerical results for the −10 dB lateral resolution, the −20 dB axial resolution and the contrast are given in A.3.

The lateral resolution tended to get worse when CCC was applied. In the axial direction, CCC evened out the distinct peaks reported in section 4.2.2 (Fig. 16) and to some degree decreased the width of the main lobe for many angle combinations and axial velocities above 3 cm/s. However, as illustrated by the axial beam profiles in Fig. 20, CCC increased the intensity of the range sidelobe, resulting in an extremely poor resolution for some angle selections and sequences. The AP sequence in combination with CCC technique seemed to maximize the intensity of the range sidelobe. For some tilt angle combinations, such as decimation factor 1, maximum angle 13.6° and angle sequence AP for a scatterer moving at 5 cm/s axially, the CCC increased the intensity of the range sidelobe to such an extent that it exceed the intensity of the actual point scatterer. This is shown in Fig. 20b.

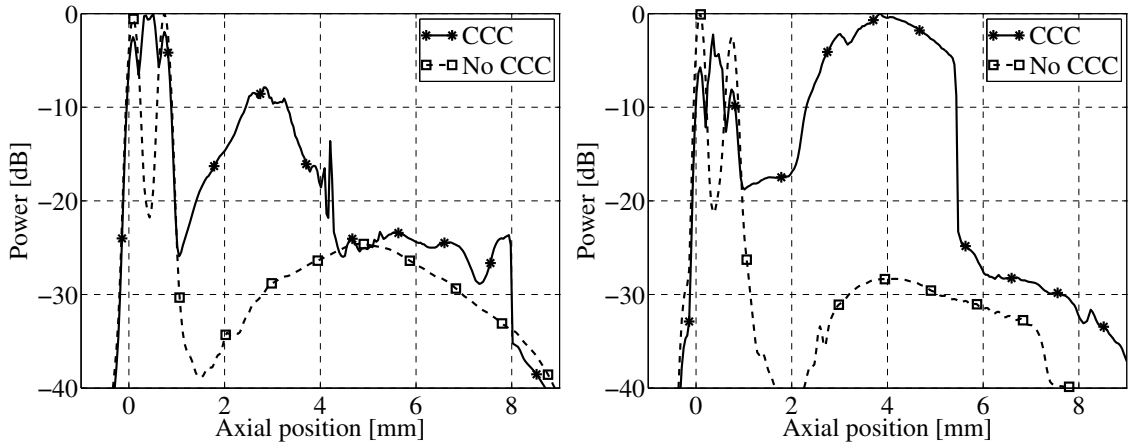

(a) LA (b) AP

Figure 20: Axial beam profiles for simulated point scatterer moving at 5.0 cm/s *axially, using (a) LA and (b) AP both using CCC and not. Decimation factor* 1 *and maximum angle* 13.6° *($F_{\#}$ 2.1) has been used*

In Figs. 17c and d CCC corrected images are shown. The gaps between the distinct peaks are filled, but the intensity of the range sidelobes is increased. There is also increased intensity on the edges of the image as a consequence of CCC.

Fig. 21 shows some simulated cysts both with and without CCC. The only effect is slightly more clutter inside the cyst for the corrected cysts.

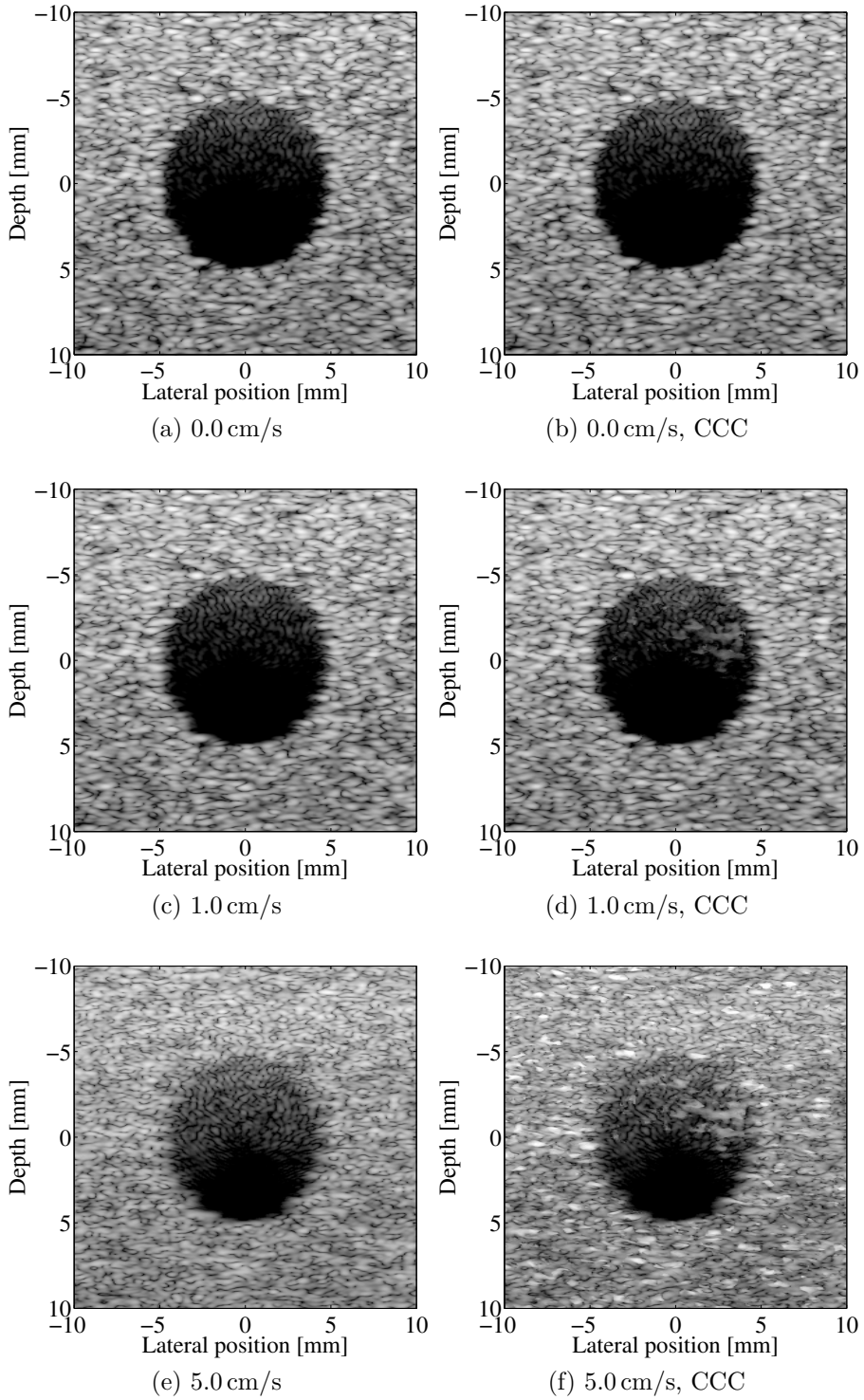

(a) 0.0 cm/s (b) 0.0 cm/s, CCC

(c) 1.0 cm/s (d) 1.0 cm/s, CCC

(e) 5.0 cm/s (f) 5.0 cm/s, CCC

Figure 21: Simulated cyst images for scatterers surrounding non-echoic cyst moving at 0.0 *((a) and (b)),* 1.0 *((c) and (d)) and* 5.0 cm/s *((e) and (f)) axially with and without CCC. Decimation factor* 2*, maximum angle* 13.6° *($F_\#$* 2.1*) and the AP sequence have been used. Dynamic range* 50 dB*. The gain has been adjusted for better comparison.*

4.3 *In vivo* measurements

Images from measurements of a rat heart are shown in Fig. 22 for coherent plane-wave compounding using the full set of angles (first row in Table 1) in the AP sequence and for a conventional fixed-focus of 20 mm. All rat images are also attached digitally. The images shown are taken during the diastole (relaxation of the heart) where there is significant movement in the heart walls to the lower left of the image.

There are more bubbles in the ultrasound gel above the rat in the plane-wave acquisition, which is the result of a change of view between the measurements. The resolution is better in the plane-wave image than in the fixed-focus image, and the resolution is also good in the whole image. There are more side lobes in the plane-wave image, as can be seen particularly on the border between rat and acquisition gel, at a depth of about 15 mm.

Slow-motion movies have been made for all decimation factors and both sequences to better see the effect of decimation and sequence selection. The movies (digitally attached) have frame rates of 4, 13, 26, 52 and 104 fps for fixed-focus, decimation factor 1, 2, 4 and 8, respectively, which is 1/15th of the acquisition frame rates. In Fig. 23, images from acquisitions with decimation factors 1, 2 and 4, using both angle sequences LA and AP and both with and without motion correction by the CCC technique are shown. These images are also taken from the diastole. As the data for the individual angle selections come from different measurements and no ECG synchronization is available, a choice of frame for the different decimation factors has been performed manually to compare the images.

There are no strong motion artifacts present in plane-wave measurements, but some flickering is visible in the attached movies.

For decimated acquisitions, effects similar to grating lobes could be seen as moving artifacts away from the moving part of the heart. For decimation factor 2 (Figs. 23c and d), the intensity of these grating lobes was low compared to the intensity of the corresponding main lobes. Using an appropriate gain, the visibility of the grating lobes was limited.

A decimation factor of 4 (Figs. 23e and f) introduced even more grating lobes and a significantly degraded contrast. Increasing the decimation further to a factor of 8 makes the aorta (middle left) completely unrecognizable.

The correlation of the *in vivo*-images turned out to be too low to use the normalized correlation limit of 0.97 used in the simulations (section 3.5). The correlation limit was set to 0.90 for the CCC images shown in Figs. 23g to l. Still, only some areas had a correlation coefficient higher than the limit, mainly the stationary part of the heart. Thus, the effect was limited and did not produce any improvement.

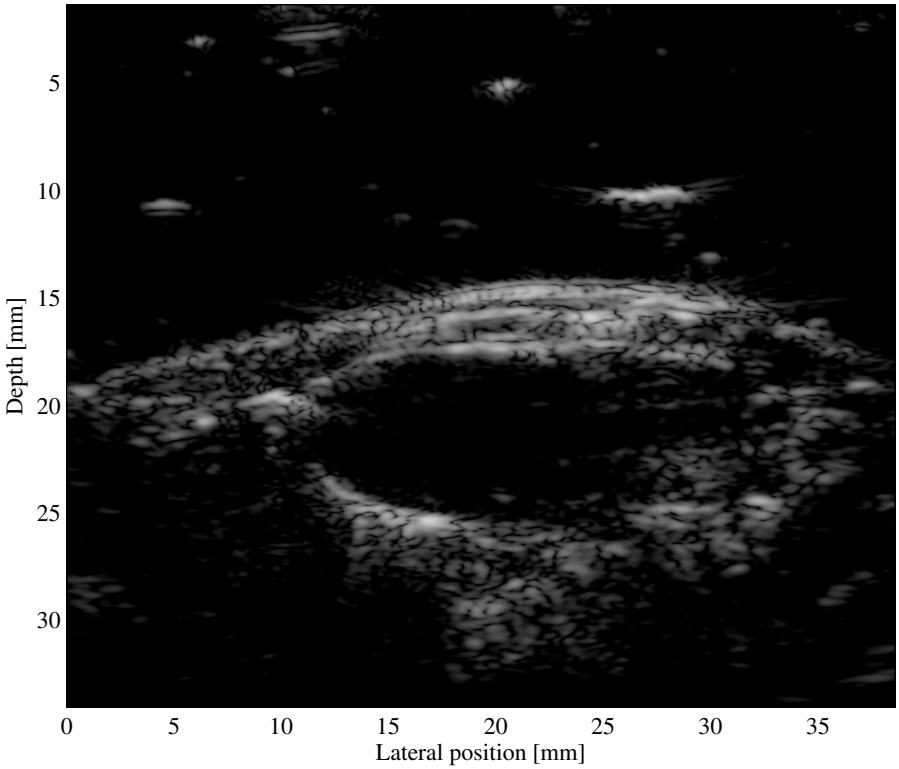

(a) Plane-wave compound, AP

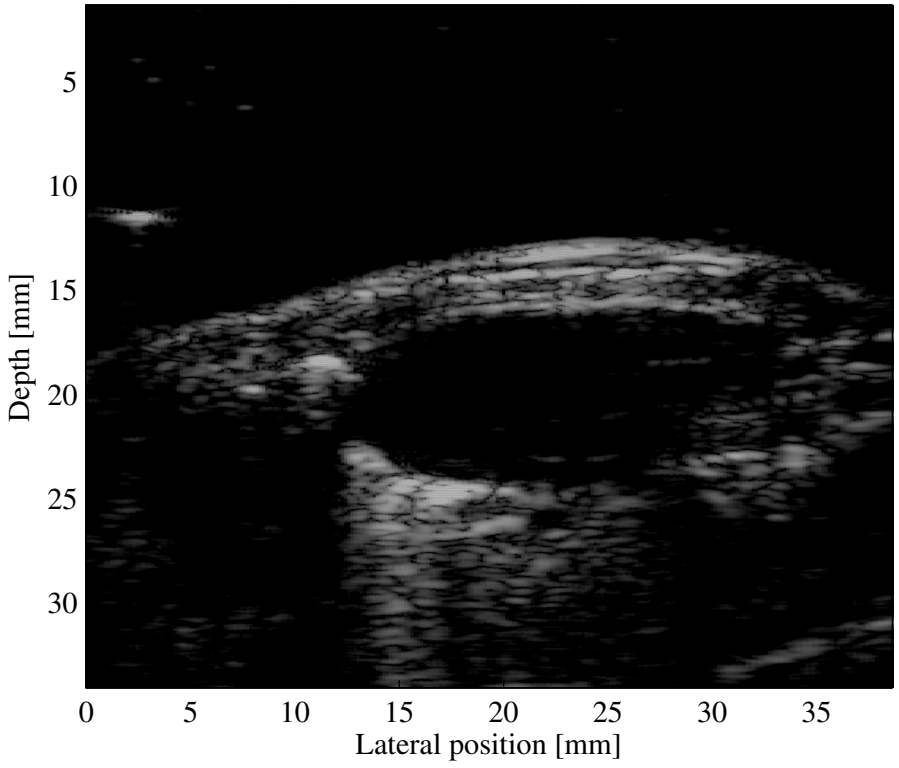

(b) Fixed-focus

Figure 22: Parasternal long axis view of a young rat's left ventricle (a) using the optimal coherent plane-wave compound in the AP sequence and (b) using a fixed transmit focus of 20 mm. *The apex is to the left in the images, while the aortic and mitral valves are to the right.*

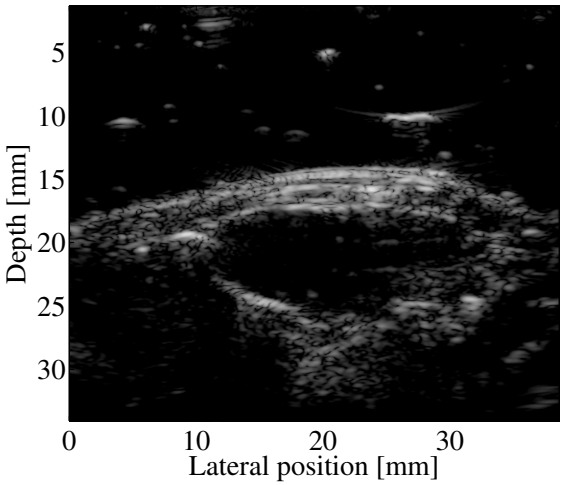

(a) Dec 1, LA sequence

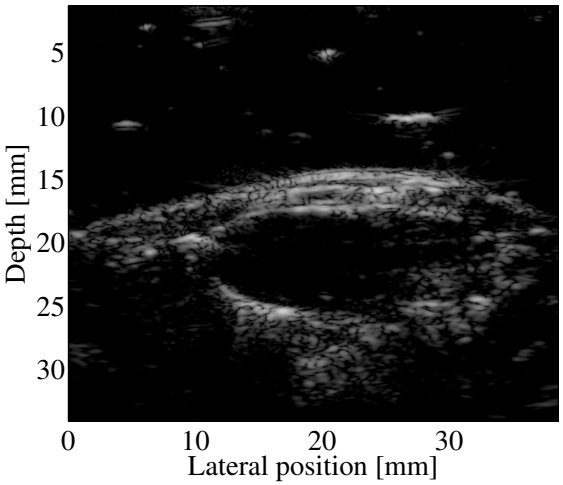

(b) Dec 1, AP sequence

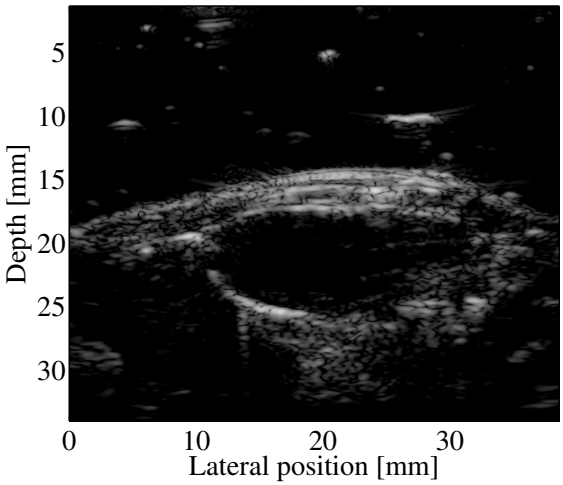

(c) Dec 2, LA sequence

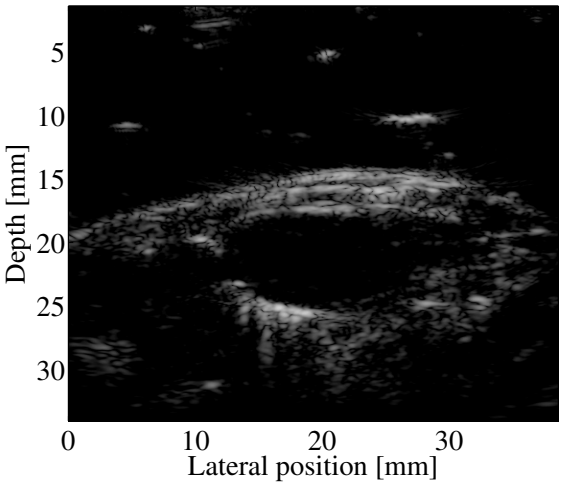

(d) Dec 2, AP sequence

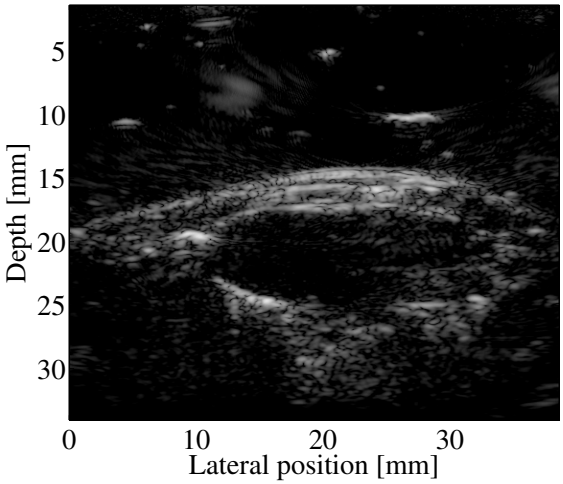

(e) Dec 4, LA sequence

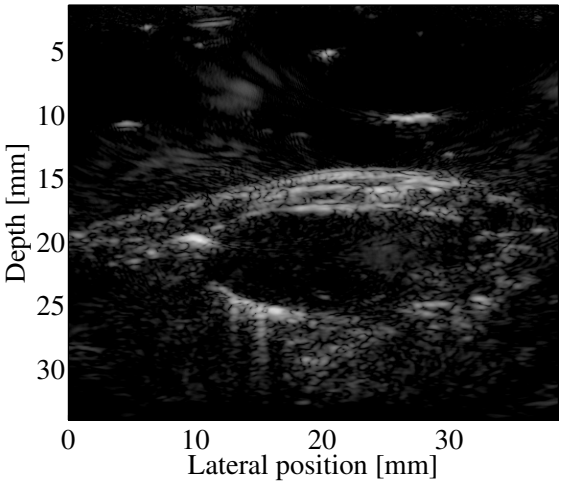

(f) Dec 4, AP sequence

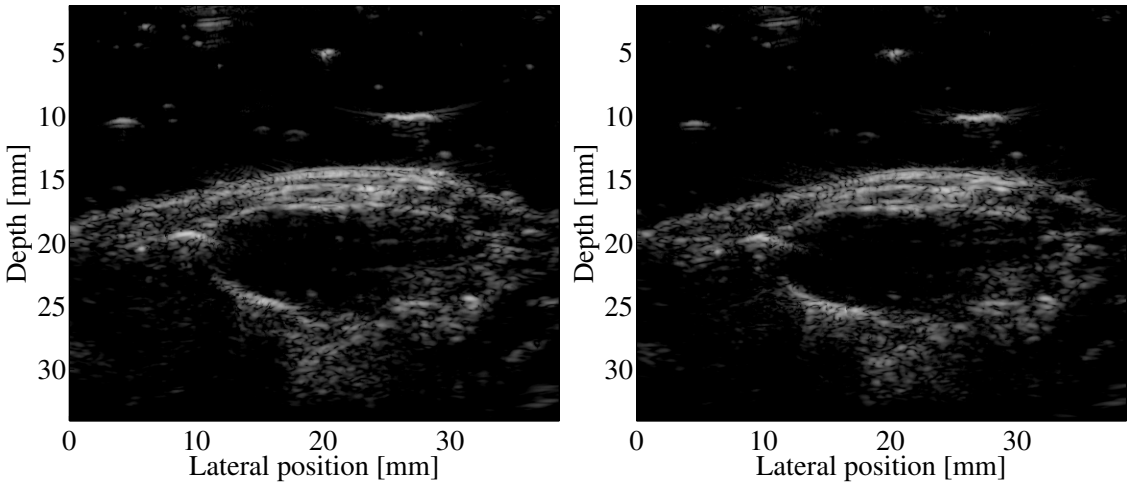

(g) Dec 1, LA sequence, CCC

(h) Dec 1, AP sequence, CCC

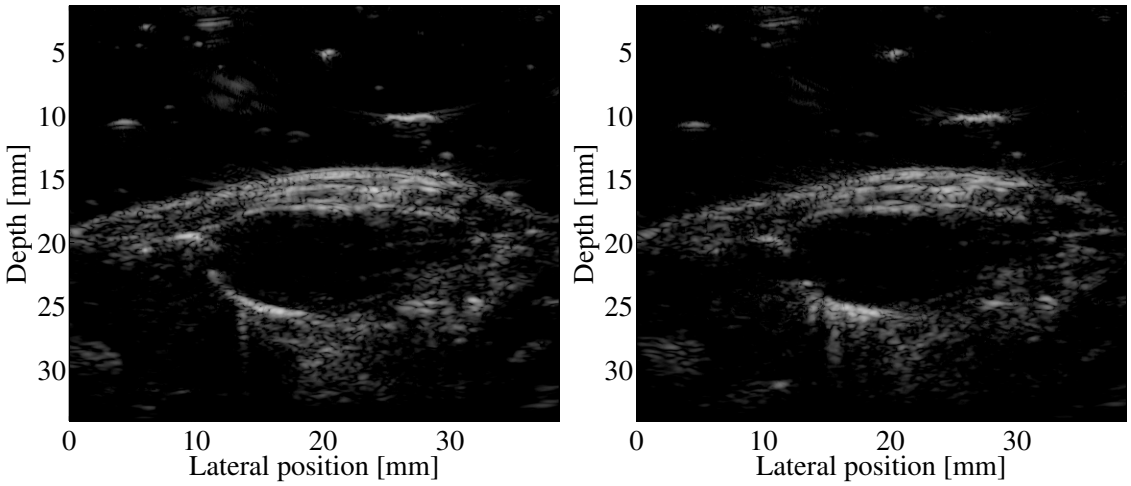

(i) Dec 2, LA sequence, CCC

(j) Dec 2, AP sequence, CCC

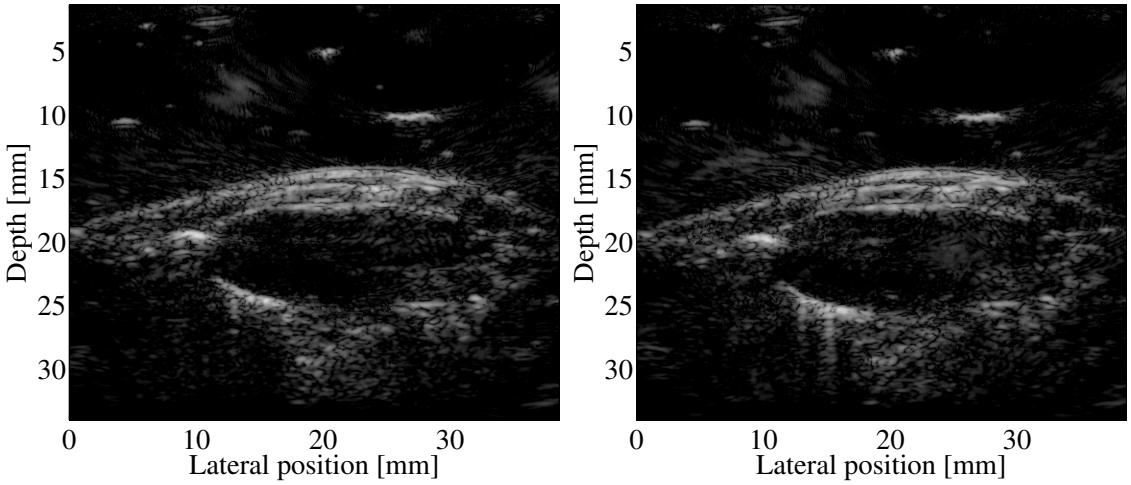

(k) Dec 4, LA sequence, CCC

(l) Dec 4, AP sequence, CCC

Figure 23: In vivo-*measurements of the parasternal long axis view of a young rat's heart for decimation factors* 1, 2 *and* 4 *using angle sequences LA and AP and CCC with a normalized correlation limit of* 0.90.

5 Discussion

5.1 Stationary objects

In previous work [26], both the lateral resolution and contrast of the optimal plane wave compound were found to be slightly worse than the optimally transmit focused fixed-focus technique. This was contrary to the results reported by Montaldo et al. [2], where the image quality of the coherent plane-wave compound completely matched that achieved at the focal depth of fixed-focus acquisitions. The results presented here are more equal to the latter results [2], as the lateral resolution of the coherent plane-wave compound at a given depth does not deviate more than 0.12 mm from the fixed-focus resolution for neither simulations nor *in vitro* measurements. This maximum deviation was found for *in vitro* measurements at 50 mm depth, were the receive F-number for the fixed-focus acquisitions was higher than the desired F-number of 2. Thus, a slightly degraded resolution for the conventionally focused waves was to be expected at this depth. Excluding this depth, the maximum difference is 0.10 mm.

These results are expected from a theoretical point of view as the pressure field of a compound of plane waves tilted at optimal angles equals the pressure field of fixed-focus waves, as shown in section 2.9.1.

Compared to the simulations presented in [26], several parameters have changed in the generation of the present simulated results. Firstly, Hamming apodization was applied on both fixed-focus and plane-wave simulations in the present report, and secondly, parameters matching those of the L9 transducer were used. However, both of these factors applies to both the conventionally and synthetically focused simulations, and should not influence the achieved resolution relative to the other technique. Thirdly, both lateral resolution and contrast was calculated differently, which again affects equally both transmission methods.

Lastly, while the generation of fixed-focus waves has stayed the same, adjustments have been made to the simulation of the coherent plane-wave compound. On the transmit side, the focal depth of the plane waves has been extended from 1.0 m to 5.0 m as it turned out that the waves were not plane enough. In the receive beamforming some delay errors have been fixed, so that the simulated results in this report resembles more closely the real situation. This is also validated by the *in vitro* measurements.

The contrast results from simulations and measurements also confirmed the equivalence of the two beamforming techniques with little difference in contrast. While the plane-wave compound gave the best results in the simulations, the best contrast for the *in vitro* measurements was found for the fixed-focus method, but non of the results deviated more than 3.0 dB. Again, this was expected from theory (section 2.9.1).

5.1.1 Reduced angle selection

The lateral resolution of the coherent plane-wave compound for varying angles for both simulations and *in vitro* measurements showed a linear dependence on the maximum transmit angle used, with the best results achieved for higher maximum angles. The decimation factor introduced only minor differences, with some resolution improvement with increasing decimation factor. This confirms to a large degree the theoretical derivations in section 2.9.1. According to (17), the F-number is in inverse ratio to the maximum angle. As a low F-number means a good lateral resolution, an improvement would be expected for high maximum angles. In addition, as the maximum angle relates to the maximum spatial frequency in the lateral direction through (8), it seems reasonable that a lower maximum angle should reduce the abruptness of imaging changes in the lateral direction, which reduces the resolution.

According to (19) and Fig. 4, the shape of the main lobe of the pressure field at focal depth does not change much as a function of decimation factor. This is supported by the minimal resolution change in the simulations and measurements caused by decimation compared to reduced maximum angle. (19) does not, however, explain that there is some resolution improvement by decimation.

Both simulations and measurements show degradation of image contrast as the decimation factor is increased. This is a logical effect of the decimation dependent grating lobes displayed in Fig. 4. The degree of degradation due to decimation is different for the simulated and the measured results, as well as the effect of maximum angle. While the maximum angle seems to be a minor influence on the contrast for *in vitro* measurements, with some, but limited, contrast improvement for a higher maximum angle, the simulated results show more effect of a varying maximum angle, with the best results achieved using the lowest maximum angle, contrary to the *in vitro* results.

Looking at (18), the effect of reducing the maximum angle, corresponding to a lower N, is a widening of the numerator sine, which should lead to a degradation of contrast, rather than improvement, as was the case for the simulations.

Using the results from the *in vitro* measurements, reducing the number of angles from 83 to 49 by reducing the maximum angle from 14.1° to 8.2° ($F_\#$ 2.0 to 3.5) leads to a degradation in lateral resolution of 0.26 mm from 0.85 to 1.11 mm and a degradation in contrast of 2.3 dB from −27.0 to −24.7 mm.

Reducing the number of angles to 41 by applying a decimation factor of 2, which includes reducing the maximum angle from 14.1° to 13.7°, leads to no change in lateral resolution, and only an insignificant degradation in contrast of 0.5 dB from −27.0 to −26.5 dB.

A combination of the two using a decimation factor of 2 and a maximum angle reduction from 14.1° to 11.0° ($F_\#$ 2.0 to 2.6) leads to a 0.11 mm wider −10 dB width than the optimal angle selection and a contrast reduction of 1.5 dB, which is worse than the results achieved using the 41 angles from above, with a reduction of no more than 8 angles.

The unapodized lateral beam profiles showed clear grating lobes for decimation

factors 4 and 8. According to (18) and Fig. 4, side lobes should appear at a relative distance of $\frac{x'}{L} = \frac{1}{D}$ (symbols as in section 2.9.1), which for factors 4 and 8 is 0.25 and 0.13, slightly closer than the measured 0.31 and 0.14. The difference could be a result of many things, such as rounding errors in the beamforming and the use of approximated angles.

5.2 Moving objects

Simulations confirm that moving scatterers reduce the image quality when the coherent plane-wave compound is applied. The degree of resolution degradation is determined by multiple factors.

All results indicated less effect of lateral motion than of axial motion, which is in agreement with section 2.10.

The sequence in which the tilt angles are used is important. Both investigated sequences introduced side lobes due to the regular intervals between angles as predicted in section 2.10.1. This may be less important in a real acquisition situation, when the motion and scatterer pattern is more complicated. Several angle sequences are possible, all of which have some good and some bad qualities which vary according to velocity. A suggestion might be to use a random sequence of a symmetric sequence with varying angle spacing to eliminate the side lobes present for the LA and AP sequences.

Compared to the LA sequence, the AP sequence has a favorable symmetric point spread function as well as lower side lobes due to the fact that they separate to both sides of the point. On the other hand, the intensity of the range side lobe is lower for the LA sequence of most investigated velocities.

The contrast simulations indicated little difference in contrast between the two sequences, except for decimation factor 2 and velocity 10.0 cm/s. There reason for the sudden contrast degradation for this angle selection in the LA sequence is not known, but it is reasonable to assume that it is connected to the high range side lobe seen in Fig. 16e in section 4.2.4. However, the range side lobe has an equally high intensity for the AP sequence, without the effect on the contrast.

The contrast loss due to motion was less for larger decimation factors than for decimation factor 1. As the contrast for a stationary scatterer is worse for larger decimation factors, the contrast is still superior for decimation factor 2, where the difference in contrast loss is less than the difference for stationary scatterers. For a decimation factor of 4, on the other hand, the very limited contrast loss due to scatterer velocity ensures a better contrast using this decimation factor than without decimation for velocities above 5.0 cm/s. For the AP sequence, the difference in contrast between sequences decimated with factors 1 and 2 decrease toward higher velocities, which may indicate that for even higher velocities, the contrast is superior for decimation factor 2. This happens when the advantage of fewer angles weighs up for the disadvantage of grating lobes for larger decimation.

It was believed that some of the effect of motion could be compensated for by using only a subset of angles to reduce the total displacement per frame. This was not generally the case, but for decimation factor 4 using the LA sequence, both

lateral and axial resolution and contrast values were better than for decimation factor 1 for the maximum investigated velocity. A decimation factor of 2 was not enough reduction in number of angles to yield better contrast results.

There was some improvement by decimation for selected axial resolutions, but the high intensity of the range side lobe prevented this for many simulations. The lateral resolution varied to such an extent with all parameters that there is no general rule for the effect of reduced number of angles.

Both contrast and axial resolution were improved by lowering the maximum angle.

5.2.1 Motion correction

The simulations showed that the CCC technique as it was implemented in the present simulations has little value as a tool to reduce motion artifacts. Although the axial resolution in particular did improve for some simulations, the general effect of CCC was reduced image quality.

The goal of CCC is to reduce the phase lag at the scatterer position caused by motion. However, as the relative phase of the individual waves is essential in reducing the signal away from the scatterer by destructive interference, reducing this phase lag may lead to constructive interference where cancellation of echoes is preferred. This effect is responsible for the degraded lateral resolution and higher intensity side lobes when using CCC.

For a single point scatterer, it would be desirable to limit the correction to a small area covering the scatterer to reduce the unwanted phase correction at other locations. This could be done using coordinates or discrimination on intensity. For *in vivo* measurements, this is not possible, but a strong signal from a scatterer may prevent the correction of signal from a more distant scatterer.

As seen in section 2.10, an axial velocity of 8.6 mm leads to a relative phase displacement of π when transmitting 81 angles per frame. A velocity of 10.0 cm/s corresponds to a relative phase of more than 11π between first and middle transmitted wave. This is much more than the limit for possible correction, and hence CCC could not work as it was supposed to. However, the quality reduction due to motion for velocities below 8.6 mm is insignificant, and no correction is necessary for such velocities.

If the number of angles is reduced, the maximum velocity which gives a phase difference of less than π is increased. A decimation factor of 8 increases the maximum velocity to 34.4 mm, but at the loss of image contrast. The gain in maximum velocity for a decimation factor of 2 is not significant enough to be relevant.

5.3 *In vivo* measurements

The *in vivo* measurements presented in this report shows that the coherent plane-wave compounding is capable of imaging moving tissue without significant artifacts. The resolution and the frame rate achieved using the optimal plane-wave selection was superior to the fixed-focus measurements. As long as the sampling criteria is

fulfilled, the plane-wave compounded images may be upsampled as much as needed, while the number of lateral samples is limited by the number of transmitted beams per frame for the fixed-focus method.

The resolution was equal in all parts of the heart, confirming the theory in section 2.9.1 and the simulations and *in vitro*-measurements presented in section 4.

There was also a degraded contrast caused by angle decimation and the accompanying grating lobes, which correspond to the theory and simulations.

6 Further work

The coherent plane-wave compound shows promising results and should be considered in the future. However, there is still much to improve.

Applying apodization on transmit beams may reduce the side lobes seen in Fig. 4 at the cost of a wider main lobe. As shown in (11) and (13), apodization weights on the individual plane waves correspond to apodization weights on the individual transmit elements for the fixed-focus case. In this respect, a high maximum angle corresponds to an element toward the ends of the active aperture.

Another improvement could be to look further into motion correction. One possibility is to apply CCC between each pair of transmitted waves to do phase correction in smaller steps. This increases the maximum velocity that can be corrected, as the phase shift between only two successive waves is the limiting factor. This does not improve the ability of CCC to distinguish phase lags caused by motion and phase lags caused by angle differences, which may or may not continue to be a problem.

In order to improve the quality of rat heart images, a more high-frequent transducer is necessary. Such a transducer will be available at the institute shortly, which will enable competitive imaging of small, moving objects.

Real time imaging is not yet possible. Tailored systems to handle large amounts of data and post-processing must be present for easier and quicker viewing of images acquired using the coherent plane-wave technique.

7 Concluding remarks

The results presented in this report from both simulations, *in vitro* and *in vivo* measurements confirmed the ability of the coherent plane-wave compound to focus at all points in the image with an increase in frame rate compared to conventional fixed-focus acquisitions. Both the lateral resolution and contrast results for both simulated and measured point scatterers and cysts of the optimal plane-wave compound matched the results achieved at the focal depth of fixed-focus transmissions.

The results from simulations and *in vitro* measurements did not agree on the influence of F-number on the contrast or the degree of contrast change by increasing the tilt angle increment, but both sets of results indicated that an increased transmit F-number degrades the lateral resolution, while a larger angle increment degrades the contrast.

The achievable frame rate can be doubled to reach 300 fps (using a PRF of 12 kHz) by doubling the angle increment from 0.34° to 0.68°, reducing the number of tilt angles from 81 to 41, or by decreasing the maximum angle from 13.6° to 8.2° ($F_{\#}$ 2.1 to 3.5), which results in 49 tilt angles. The quality loss due to these reductions is not clear from the deviating simulated and measured results, but the contrast reduction in the first approach should not exceed 11 dB (25 %) and the resolution degradation in the second approach should not exceed by 0.3 mm (30 %).

The effect of motion on plane-wave acquisitions where found to be significant for simulated point scatterers with axial velocities, but not so for lateral velocities. The sequence of plane-wave tilt angles proved to be important for the image quality. Several factors influenced the contrast and resolution degradation, and the optimal choice of sequence and angle selection is application dependent. The quality degradation due to motion was decreased for a decimation factor of 4, but not for decimation factor 2.

The same motion artifacts were not found for *in vivo* measurements where the scatterer pattern is more complex. On the other hand, these measurements showed that a decimation factor of 4 or more significantly reduces image quality due to grating lobes.

The coherent plane-wave compound is a promising technique for high quality, high frame rate imaging of moving objects and should be investigated further.

References

[1] K. T. Song and J. H. Chang, "Synthetic aperture focusing method for ultrasound imaging based on planar waves," US Patent US 6 736 780, 2004.

[2] G. Montaldo, M. Tanter, J. Bercoff, N. Benech, and M. Fink, "Coherent plane-wave compounding for very high frame rate ultrasonography and transient elastography." *IEEE Transactions on Ultrasonics, Ferroelectrics and Frequency Control*, vol. 56, pp. 489–506, 2009.

[3] B. Delannoy, R. Torguet, C. Bruneel, E. Bridoux, J. M. Rouvaen, and H. Lasota, "Acoustical image reconstruction in parallel-processing analog electronic systems," *Journal of Applied Physics*, vol. 50, pp. 3153–3159, 1979.

[4] C. Bruneel, E. Bridoux, B. Delannoy, B. Nongaillard, J. M. Rouvaen, and R. Torguet, "Effect of spatial sampling on an acoustical image reconstruction," *Journal of Applied Physics*, vol. 49, pp. 569 – 573, 1978.

[5] J. Bercoff, G. Montaldo, T. Loupas, D. Savery, F. Mézière, M. Fink, and M. Tanter, "Ultrafast compound Doppler imaging: providing full blood flow characterization." *IEEE Transactions on Ultrasonics, Ferroelectrics and Frequency Control*, vol. 58, pp. 134–147, 2011.

[6] B. A. J. Angelsen, *Ultrasound Imaging. Waves, Signals and Signal Processing.* Emantec, 2000.

[7] T. L. Szabo, *Diagnostic ultrasound imaging: inside out.* Academic Press, 2004.

[8] K. K. Shung and M. Zippuro, "Ultrasonic transducers and arrays," *IEEE Engineering in Medicine and Biology Magazine*, vol. 15, pp. 20–30, 1996.

[9] J. N. Wright, "Image formation in diagnostic ultrasound," *1997 IEEE International Ultrasonic Symposium Short Course*, http://folk.ntnu.no/hergum/medt8012/WrightCompendium.pdf, 1997.

[10] K. E. Thomenius, "Evolution of ultrasound beamformers," in *1996 IEEE Ultrasonics Symposium. Proceedings*, vol. 2. IEEE, 1996, pp. 1615–1622.

[11] D. S. S. Kreindler, "Beamforming in medical ultrasound," http://www2.electronicproducts.com/Beamforming_in_medical_ultrasound-article-MedAppFocus_Samplify_Feb2011-html.aspx, Samplify Systems, 2011.

[12] "Medical imaging - Ultrasound imaging systems," http://www.maxim-ic.com/solutions/guide/medical/Ultrasound.pdf, Maxim, 2012.

[13] S. A. Tretter, "Bandpass Signal Representation," http://www.ece.umd.edu/class/enee429w.F99/bandpass.pdf, University of Maryland, 1999.

[14] J. Kirkhorn, "Introduction to IQ-demodulation of RF-data," http://folk.ntnu.no/htorp/Undervisning/TTK10/IQdemodulation.pdf, 1999.

[15] J. G. Proakis and D. G. Manolakis, *Digital signal processing.* Pearson Prentice Hall, 2007.

[16] B. Denarie, H. Torp, and G. Haugen, "Motion Compensated Synthetic Transmit Beam Technique for Real-time Echocardiography," in *2011 IEEE International Ultrasonics Symposium.* IEEE, 2011, pp. 136–139.

[17] G. S. Kino, *Acoustic Waves, Devices Imaging and Analog Signal Processing.* Prentice Hall, 1987.

[18] T. Hergum, T. Bjastad, K. Kristoffersen, and H. Torp, "Parallel beamforming using synthetic transmit beams," *IEEE Transactions on Ultrasonics, Ferroelectrics and Frequency Control*, vol. 54, pp. 271–280, 2007.

[19] J.-Y. Lu, "2D and 3D high frame rate imaging with limited diffraction beams," *IEEE Transactions on Ultrasonics, Ferroelectrics and Frequency Control*, vol. 44, pp. 839–856, 1997.

[20] ——, "Experimental study of high frame rate imaging with limited diffraction beams." *IEEE Transactions on Ultrasonics, Ferroelectrics and Frequency Control*, vol. 45, pp. 84–97, 1998.

[21] C.-L. Hu, G.-S. Jeng, Y.-H. Wang, P.-C. Li, and M.-L. Li, "Improved plane-wave high frame rate imaging using retrospective transmitfocusing and filter-derived coherence-index weighting," in *2010 IEEE International Ultrasonics Symposium, Proceedings*, 2010, pp. 1916–1919.

[22] J. Cheng and J.-Y. Lu, "Extended high-frame rate imaging method with limited-diffraction beams," *IEEE Transactions on Ultrasonics, Ferroelectrics and Frequency Control*, vol. 53, pp. 880–899, 2006.

[23] J. A. Jensen, "FIELD: A Program for Simulating Ultrasound Systems," in *10th Nordic-Baltic Conference on Biomedical Imaging*, 1996, pp. 351–353.

[24] MATLAB, *Version 7.7.0.421 (R2008b).* The MathWorks Inc., 2008.

[25] C. Weytjens, B. Cosyns, J. D'hooge, C. Gallez, S. Droogmans, T. Lahoute, P. Franken, and G. Van Camp, "Doppler myocardial imaging in adult male rats: reference values and reproducibility of velocity and deformation parameters." *European journal of echocardiography*, vol. 7, pp. 411–417, 2006.

[26] R. Øvland, "Coherent plane-wave compounding on simulated ultrasound B-mode images," TFY4510 Project report, NTNU, 2011.

A Numerical results

A.1 Stationary objects

A.1.1 Simulations

Table A.1: −10 dB *lateral resolution of simulated stationary point scatterer placed at depths* 20*,* 25*,* 30*,* 35*,* 40*,* 45 *and* 50 mm *for the optimal plane-wave combination (row 1 in Table 1) and for fixed-focused waves focusing at* 20*,* 30*,* 40 *and* 50 mm*.*

	Lateral resolution [mm]						
	20 mm	25 mm	30 mm	35 mm	40 mm	45 mm	50 mm
Plane wave	0.67	0.68	0.70	0.72	0.75	0.79	0.81
Foc. depth 20 mm	0.70	1.08	1.40	1.42	1.34	1.29	1.30
Foc. depth 30 mm	1.20	1.21	0.70	1.17	1.51	1.34	1.29
Foc. depth 40 mm	1.23	1.25	1.22	1.19	0.74	1.19	1.55
Foc. depth 50 mm	1.23	1.25	1.28	1.31	1.31	1.19	0.77

Table A.2: Contrast for simulated stationary cyst placed at depth 30 mm *for the optimal plane-wave combination (row 1 in Table 1) and for fixed-focused waves focusing at* 20*,* 30*,* 40 *and* 50 mm*.*

	Contrast [dB]
Plane wave	−39.1
Foc. depth 20 mm	−37.9
Foc. depth 30 mm	−36.1
Foc. depth 40 mm	−35.7
Foc. depth 50 mm	−38.8

Table A.3: −10 dB *lateral resolution for simulated stationary point scatterer placed at depth* 30 mm *for several plane-wave combinations of decimation factors* 1 - 8 *and maximum angles* 8.2°*,* 10.9° *and* 13.6° *($F_\#$* 3.5*,* 2.6 *and* 2.1*) (rows 2-4 in Table 1).*

	Lateral resolution [mm]		
	2.1	2.6	3.5
Dec. factor 1	0.72	0.84	0.98
Dec. factor 2	0.72	0.84	0.98
Dec. factor 4	0.71	0.82	0.96
Dec. factor 8	0.69	0.79	0.92

Table A.4: Contrast for simulated stationary cyst placed at depth 30 mm *for several plane-wave combinations of decimation factors* 1 - 8 *and maximum angles* 8.2°, 10.9° *and* 13.6° *($F_\#$* 3.5, 2.6 *and* 2.1*)(rows 2-4 in Table 1).*

	Contrast [dB]		
	2.1	2.6	3.5
Dec. factor 1	-39.2	-39.5	-40.4
Dec. factor 2	-27.8	-30.7	-33.2
Dec. factor 4	-27.1	-30.0	-32.6
Dec. factor 8	-23.4	-24.9	-26.2

A.1.2 *In vitro* measurements

Table A.5: −10 dB *lateral resolution of* in vitro *stationary point scatterer placed at depths* 20, 30, 40, *and* 50 mm *(*47 mm *for fixed-focus measurements) for the optimal plane-wave combination (row 1 in Table 1) and for fixed-focused waves focusing at* 20, 30, 40 *and* 47 mm.

	Lateral resolution [mm]			
	20 mm	30 mm	40 mm	50 mm
Plane wave	0.85	0.85	0.88	0.93
Foc. depth 20 mm	1.23	0.84	1.65	2.29
Foc. depth 30 mm	1.24	1.35	0.98	1.27
Foc. depth 40 mm	1.12	1.34	1.78	1.10
Foc. depth 47 mm	0.76	0.84	0.98	1.10

Table A.6: Contrast for in vitro *stationary cyst placed at depth* 30 mm *for the optimal plane-wave combination (row 1 in Table 1) and for fixed-focused waves focusing at* 10, 20, 30 *and* 40 mm.

	Contrast [dB]
Plane wave	−26.8
Foc. depth 10 mm	−28.6
Foc. depth 20 mm	−25.5
Foc. depth 30 mm	−19.7
Foc. depth 40 mm	−18.4

Table A.7: −10 dB *lateral resolution for* in vitro *stationary point scatterer placed at depth* 30 mm *for several plane-wave combinations of decimation factors* 1 - 8 *and maximum angles* 8.2°, 10.9° *and* 13.6° *($F_\#$* 3.5, 2.6 *and* 2.1*) (rows 2-4 in Table 1).*

	Lateral resolution [mm]		
	2.1	2.6	3.5
Dec. factor 1	0.86	0.97	1.11
Dec. factor 2	0.85	0.96	1.10
Dec. factor 4	0.84	0.94	1.08
Dec. factor 8	0.83	0.91	1.05

Table A.8: Contrast for in vitro *stationary cyst placed at depth* 10 mm *for several plane-wave combinations of decimation factors* 1 - 8 *and maximum angles* 8.2°, 10.9° *and* 13.6° *($F_\#$* 3.5, 2.6 *and* 2.1*)(rows 2-4 in Table 1).*

	Contrast [dB]		
	2.1	2.6	3.5
Dec. factor 1	-26.7	-25.7	-24.5
Dec. factor 2	-26.3	-25.3	-24.0
Dec. factor 4	-14.1	-13.4	-12.3
Dec. factor 8	-12.2	-11.4	-10.4

A.2 Movement

Table A.9: −10 dB *lateral resolution, simulated point scatterer at* 20 mm *depth with axial and lateral velocities from* 0 - 10.0 cm/s *for decimation factors* 1 *and* 2*, maximum angles* 13.7° *and* 8.2° *($F_\#$* 2.1 *and* 3.5*) and angle sequences LA and AP.*

		Lateral resolution [mm]					
		Dec. factor 1		Dec. factor 2		Dec. factor 4	
		LA	AP	LA	AP	LA	AP
$F_\#$ 2.1	0 cm/s	0.69	0.69	0.69	0.69	0.67	0.67
	1 cm/s ax.	0.68	1.11	0.68	0.75	0.67	0.69
	3 cm/s ax.	1.24	1.09	0.67	1.54	0.67	0.89
	5 cm/s ax.	1.59	1.33	1.12	1.50	0.66	1.37
	10 cm/s ax.	1.34	1.29	1.29	1.25	1.12	1.45
	5 cm/s lat.	0.78	0.74	0.70	0.70	0.67	0.68
	10 cm/s lat.	1.16	0.94	0.77	0.74	0.69	0.69
$F_\#$ 3.5	0 cm/s	0.94	0.94	0.93	0.93	0.91	0.91
	1 cm/s ax.	0.92	0.99	0.92	0.94	0.91	0.91
	3 cm/s ax.	1.19	1.73	0.90	1.08	0.91	0.94
	5 cm/s ax.	1.45	1.00	0.90	1.50	0.89	1.01
	10 cm/s ax.	1.32	1.16	1.42	1.03	0.89	1.56
	5 cm/s lat.	0.94	0.95	0.93	0.94	0.91	0.91
	10 cm/s lat.	1.01	1.00	0.94	0.95	0.91	0.92

Table A.10: -20 dB *axial resolution, simulated point scatterer at* 20 mm *depth with axial and lateral velocities from* 0 - 10.0 cm/s *for decimation factors* 1 *and* 2*, maximum angles* 13.7° *and* 8.2° *(*$F_\#$ 2.1 *and* 3.5*) and angle sequences LA and AP.*

		Axial resolution [mm]					
		Dec. factor 1		Dec. factor 2		Dec. factor 4	
		LA	AP	LA	AP	LA	AP
$F_\#$ 2.1	0 cm/s	0.38	0.38	0.38	0.38	0.38	0.38
	1 cm/s ax.	0.39	0.40	0.38	0.38	0.38	0.38
	3 cm/s ax.	0.55	0.59	0.41	0.44	0.39	0.39
	5 cm/s ax.	0.74	0.73	0.49	4.9	0.40	0.42
	10 cm/s ax.	1.10	1.07	6.33	5.41	0.50	5.02
	5 cm/s lat.	0.38	0.38	0.38	0.38	0.38	0.38
	10 cm/s lat.	0.38	0.38	0.38	0.38	0.38	0.38
$F_\#$ 3.5	0 cm/s	0.37	0.37	0.37	0.37	0.38	0.38
	1 cm/s ax.	0.38	0.38	0.38	0.38	0.38	0.38
	3 cm/s ax.	0.46	0.49	0.39	0.39	0.38	0.37
	5 cm/s ax.	0.58	0.57	0.43	3.02	0.38	0.39
	10 cm/s ax.	0.80	0.78	5.04	3.24	0.44	3.17
	5 cm/s lat.	0.37	0.38	0.37	0.37	0.38	0.38
	10 cm/s lat.	0.37	0.37	0.38	0.38	0.38	0.38

Table A.11: Contrast for simulated moving cyst placed at depth 30 mm *for several plane-wave combinations of decimation factors* 1 - 2 *and maximum angles* 8.2°*, and* 13.6° *(*$F_\#$ 3.5 *and* 2.1*)(rows 2-4 in Table 1).*

		Contrast [dB]					
		Dec. factor 1		Dec. factor 2		Dec. factor 4	
		LA	AP	LA	AP	LA	AP
$F_\#$ 2.1	0 cm/s	-39.2	-39.2	-27.7	-27.7	-27.1	-27.1
	5 cm/s ax.	-24.4	-23.0	-19.2	-19.6	-24.6	-25.0
	10 cm/s ax.	-18.9	-17.5	-7.9	-16.0	-18.5	-18.4
$F_\#$ 3.5	0 cm/s	-40.4	-40.4	-33.2	-33.2	-32.6	-32.6
	5 cm/s ax.	-28.8	-29.7	-26.3	-26.5	-30.6	-31.3
	10 cm/s ax.	-24.3	-23.2	-16.1	-20.9	-25.6	-24.8

A.3 Motion correction

Table A.12: −10 dB lateral resolution for simulated moving cyst placed at depth 30 mm for several plane-wave combinations of decimation factors 1 - 2 and maximum angles 8.2°, and 13.6° ($F_\#$ 3.5 and 2.1)(rows 2-4 in Table 1). CCC applied.

	Lateral resolution [mm]							
	$F_\#$ 2.1				$F_\#$ 3.5			
	Dec. factor 1		Dec. factor 2		Dec. factor 1		Dec. factor 2	
	LA	AP	LA	AP	LA	AP	LA	AP
0 cm/s	0.88	0.80	0.87	0.87	1.17	1.17	1.16	1.16
1 cm/s ax.	0.82	0.80	0.86	0.77	1.06	1.01	1.13	1.01
3 cm/s ax.	1.25	1.59	0.74	1.18	0.81	1.26	0.96	0.94
5 cm/s ax.	1.33	1.28	0.63	1.66	1.69	1.56	0.84	1.09
10 cm/s ax.	1.23	1.30	1.37	1.30	1.32	1.34	1.71	1.40
5 cm/s lat.	0.94	0.77	0.88	0.75	1.14	1.01	1.15	1.01
10 cm/s lat.	1.13	0.87	0.94	0.77	1.14	1.05	1.14	1.01

Table A.13: −20 dB axial resolution for simulated moving cyst placed at depth 30 mm for several plane-wave combinations of decimation factors 1 - 2 and maximum angles 8.2°, and 13.6° ($F_\#$ 3.5 and 2.1)(rows 2-4 in Table 1). CCC applied.

	Axial resolution [mm]							
	$F_\#$ 2.1				$F_\#$ 3.5			
	Dec. factor 1		Dec. factor 2		Dec. factor 1		Dec. factor 2	
	LA	AP	LA	AP	LA	AP	LA	AP
0 cm/s ax.	0.38	0.38	0.38	0.38	0.38	0.38	0.38	0.38
1 cm/s ax.	0.39	0.41	0.39	0.39	0.38	0.38	0.38	0.38
3 cm/s ax.	4.09	5.35	0.40	4.35	0.42	4.43	0.39	0.40
5 cm/s ax.	4.19	5.40	0.48	5.33	3.53	4.81	0.40	0.43
10 cm/s ax.	4.37	5.54	5.88	5.40	4.19	4.89	4.83	4.81
5 cm/s lat.	0.38	0.39	0.38	0.39	0.38	0.38	0.38	0.38
10 cm/s lat.	0.37	0.39	0.38	0.39	0.377	0.38	0.38	0.38

Table A.14: Contrast for simulated moving cyst placed at depth 30 mm for several plane-wave combinations of decimation factors 1 - 2 and maximum angles 8.2°, and 13.6° ($F_\#$ 3.5 and 2.1)(rows 2-4 in Table 1). CCC applied.

	Contrast [dB]								
	$F_\#$ 2.1					$F_\#$ 3.5			
	Dec. factor 1		Dec. factor 2			Dec. factor 1		Dec. factor 2	
	LA	AP	LA	AP		LA	AP	LA	AP
0 cm/s	-39.2	-39.2	-27.8	-27.8	-40.4	-40.4	-33.3	-33.3	
5 cm/s ax.	-26.2	-13.1	-20.0	-14.7	-27.8	-19.1	-27.3	-24.9	
10 cm/s ax.	-21.4	-7.58	-13.3	-12.9	-26.5	-17.2	-19.2	-18.5	

B Attached files

Table B.1: Summary of attached files. Parasternal long axis view rat heart from in vivo *measurements. Description, decimation factor (dec), maximum angle (angle) and F-number, angle sequence (seq) and use of CCC are indicated in the table in addition to filename and extension (ext). Focal depth is indicated for the fixed-focus measurement.*

Filename	Description	Dec	Angle ($F_{\#}$)	Seq	CCC	Ext
dec1_LA	Still image	1	13.7° (2.1)	LA	No	.pdf, .fig
dec1_LA_CCC	Still image	1	13.7° (2.1)	LA	Yes	.pdf, .fig
dec1_AP	Still image	1	13.7° (2.1)	AP	No	.pdf, .fig
dec1_AP_CCC	Still image	1	13.7° (2.1)	AP	Yes	.pdf, .fig
dec2_LA	Still image	2	13.7° (2.1)	LA	No	.pdf, .fig
dec2_LA_CCC	Still image	2	13.7° (2.1)	LA	Yes	.pdf, .fig
dec2_AP	Still image	2	13.7° (2.1)	AP	No	.pdf, .fig
dec2_AP_CCC	Still image	2	13.7° (2.1)	AP	Yes	.pdf, .fig
dec4_LA	Still image	4	13.7° (2.1)	LA	No	.pdf, .fig
dec4_LA_CCC	Still image	4	13.7° (2.1)	LA	Yes	.pdf, .fig
dec4_AP	Still image	4	13.7° (2.1)	AP	No	.pdf, .fig
dec4_AP_CCC	Still image	4	13.7° (2.1)	AP	Yes	.pdf, .fig
optimal_LA	Still image	1	14.1° (2.1)	LA	No	.pdf, .fig
optimal_AP	Still image	1	14.1° (2.1)	AP	No	.pdf, .fig
fixed_focus	Still image		Focal depth 20 mm			.pdf, .fig
dec1_LA_mov	Movie (13 fps)	1	14.1° (2.1)	LA	No	.mp4
dec1_LA_mov_CCC	Movie (13 fps)	1	14.1° (2.1)	LA	Yes	.mp4
dec1_AP_mov	Movie (13 fps)	1	14.1° (2.1)	AP	No	.mp4
dec1_AP_mov_CCC	Movie (13 fps)	1	14.1° (2.1)	AP	Yes	.mp4
dec2_LA_mov	Movie (26 fps)	2	13.7° (2.1)	LA	No	.mp4
dec2_LA_mov_CCC	Movie (26 fps)	2	13.7° (2.1)	LA	Yes	.mp4
dec2_AP_mov	Movie (26 fps)	2	13.7° (2.1)	AP	No	.mp4
dec2_AP_mov_CCC	Movie (26 fps)	2	13.7° (2.1)	AP	Yes	.mp4
dec4_LA_mov	Movie (52 fps)	4	13.7° (2.1)	LA	No	.mp4
dec4_LA_mov_CCC	Movie (52 fps)	4	13.7° (2.1)	LA	Yes	.mp4
dec4_AP_mov	Movie (52 fps)	4	13.7° (2.1)	AP	No	.mp4
dec4_AP_mov_CCC	Movie (52 fps)	4	13.7° (2.1)	AP	Yes	.mp4
dec8_LA_mov	Movie (104 fps)	8	13.7° (2.1)	LA	No	.mp4
dec8_LA_mov_CCC	Movie (104 fps)	8	13.7° (2.1)	LA	Yes	.mp4